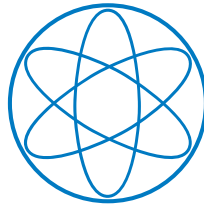


Paul Heinrich

Investigations of Alfvénic activity during the current quench in ASDEX Upgrade

IPP 2021-12
Juli 2021



Master Thesis in Physics at
Technische Universität München

Investigations of Alfvénic activity during the current quench in ASDEX Upgrade

presented by

Paul Heinrich

20th of March, Garching

First Promoter: Priv.-Doz. Dr. Ph. W. Lauber

Second Promoter: Dr. G. Birkenmeier

Supervisor: Dr. G. Papp

Contents

1	Introduction	1
1.1	Tokamak concept and ASDEX Upgrade	2
1.2	Disruptions and runaway electrons	3
1.3	Alfvén waves	10
1.4	Fourier transformations and spectrograms	15
2	Experimental Setup	17
2.1	In-vessel magnetic pick-up coils	17
2.2	Soft X-ray measurements	18
2.3	Setup for the experiments on the post-disruption modes	21
3	Mode analysis methods	23
3.1	Dijkstra’s algorithm	23
3.2	Mode tracing algorithm	25
3.3	Soft X-ray Amplitude Localization Tool – SALT	29
4	Observations and results	31
4.1	Mode characteristics	31
4.2	Mode time frame	35
4.3	Mode behaviour in incomplete disruptions	36
4.4	Localization of the modes	37
4.5	Coherence & mode numbers	40
5	Statistical analysis of the mode characteristics	41
5.1	The database	41
5.2	Most likely frequencies	44
5.3	Statistical analysis methods	45
5.4	Summary of mode characteristics for AUG	56
6	Present theories behind the current quench modes	57
6.1	Compressional Alfvén eigenmodes (CAEs)	57
6.2	Global Alfvén eigenmodes (GAEs)	58
7	Summary & Outlook	61

Acknowledgements

I want to thank all of you, who helped me during the very unusual, but interesting past year. Without you I could not have carried out my work! Even though, the whole world had to deal with the Covid-19 pandemic, I still enjoyed the time. I learned a lot and was accompanied by many very nice people!

First of all I want to thank you, Philipp. You not only enabled me to write my masters thesis at IPP, but you also contributed a lot! In multiple meetings you introduced the theory behind these modes to us and explained how the evolution of the Alfvén continuum can be interpreted. The LIGKA simulations you provided improved the overall understanding and quality of this thesis. Also I want to mention the weekly Coffee-meetings you hosted. They were not only interesting, but also provided a weekly social interaction, which is especially important during home office times.

A **HUGE** T.Hanks goes to my Supervisor Geri! Your supervision was a dream. Whenever I finished the code blocks "a bit faster" than one might expected – due to the lock-down and me enjoying coding a lot – you always had great ideas for further investigations. You are always available even though your atosecond respond time to emails sometimes felt inhuman haha. You not only provided help on a physics or supervision level, but also on a personal level. The working atmosphere you created is very, **very** enjoyable and I love having meetings with you. You definitely made this year extremely enjoyable. Even though most people will remember 2020 as "*that weird and awful year*", I will keep it in mind as an very productive **but** also nice year! Due to your positive personality, your kind words and great feedback, I am very happy working with you!

I also want to thank the all the others, who made this thesis possible:

In the beginning I had a lot of questions regarding the magnetics and SXR-diagnostic. Therefore, I want to thank Marc Maraschek and Anja Gude for your help and detailed descriptions how to handle the data acquisition of the diagnostics. A huge thanks goes to Valentin Igochine. He invested a lot of time to introduce the SXR-diagnostic and taught me a lot about SXR-physics during meetings. Also I want to thank Mike Dunne and Oliver Linder. Without your simulations, we couldn't develop our current theory behind the CQ-modes. Therefore, you provided essential pieces to the big puzzle.

However, not only colleagues from IPP contributed to this work:

Ich möchte zu aller erst meinen Eltern danken, die in der sehr einsamen und anstrengenden Coronazeit immer an meiner Seite waren. Es ist wesentlich, dass man – um produktiv zu sein – auch glücklich ist und in seiner freien Zeit zur Ruhe kommen kann. Danke, dass ihr mich immer unterstützt! Aber auch meine Freunde, mit denen man sich zwar nicht in Persona treffen konnte, aber dennoch viel Kontakt gehalten hat, möchte ich an dieser Stelle erwähnen. Dabei denke ich vor allem an Andreas, Nici und Bjarne, die immer mit Rat und Tat zur Seite standen. Besonders möchte ich Andreas aber auch dafür danken, dass er sich die Zeit für das Korrekturlesen meiner Arbeit genommen hat. Aber vor allem möchte ich meinem besten Freund danken:

Danke Jonas für alles!

Ich möchte diese Arbeit meinem Opa widmen:

Immer, wenn ich bei ihm angerufen habe, hat er sich erkundigt, wie es mit meiner Masterarbeit läuft. Man merkt, dass er nicht nur sichtbar stolz ist, sondern auch, dass er sich so sehr darüber freut, dass ich in der Physik meine Leidenschaft gefunden habe. Schon damals als ich mit meiner Bachelorarbeit und meinem ersten Paper fertig war, habe ich mich mit ihm zusammengesetzt und ihm ausführlich erklärt welche Methoden wir angewandt hatten. Ich möchte mich damit einfach bedanken, dass er mich durch seine wissbegierige Art und seine spannenden Anekdoten immer motiviert nach den Sternen zu greifen – Danke!

Chapter 1

Introduction

With the ceremony to celebrate the official start of the machine assembly phase of ITER on the 28th of July 2020, not only the media's attention has been directed towards nuclear fusion once again, but an important technological milestone has been reached. Nuclear fusion as one of the most advanced technological achievements shall provide a clean and sustainable energy supply for future generations [1, 2]. A huge variety of different fields of research – ranging from material science to magneto-hydrodynamics (MHD) – are brought together in this highly interdisciplinary project. However, despite the technological breakthroughs and the enabling research of the last decades, there are still urgent questions to answer. How to provide a highly confined plasma operation without the appearance of edge localized modes (ELMs), which deposit heat loads on the first wall [3]? How can we effectively mitigate disruptions for the next generations of fusion devices such as ITER or DEMO [4, 5, 6]? To answer open questions like these, active research is done around the globe. This thesis provides another piece of the puzzle concerning the mitigation of runaway electron (RE) generation during disruptions. In post-disruption plasmas, modes had been observed, which might have an impact on RE-generation [7, 8]. Those modes are also present in ASDEX Upgrade and their investigation is the subject of this thesis. Understanding the underlying mechanisms could lead to new RE-suppression techniques, thus advanced disruption mitigation. This thesis consists of seven chapters, starting with a short introduction. At first the tokamak concept is presented and more details on ASDEX Upgrade are given in section 1.1. This is followed by section 1.2, which covers the physics of disruptions and runaway electrons. As the nature of the post-disruption modes is expected to be Alfvénic [9], Alfvén waves are introduced in section 1.3. The time-frequency analysis via spectrograms is explained in section 1.4. In chapter 2 the experimental setup and diagnostics available at ASDEX Upgrade are presented. Chapter 3 introduces the mode analysis tools I implemented for the investigation of the post-disruption modes. The observations and results of the investigations are presented in chapter 4 and the statistical analysis in chapter 5. Our current theory behind these modes is introduced in chapter 6 and finally a summary and outlook is given in chapter 7.

1.1 Tokamak concept and ASDEX Upgrade

The acronym tokamak was derived from the Russian expression for *toroidal chamber in/with magnetic coils* [10]. The concept was first developed by two Soviet physicists Andrej Sacharow and Igor Tamm in 1952 [11, 12]. During the cold war, the Soviet union and the US competed in the development of the first nuclear fusion reactor. As a lot of progress on the tokamak concept was achieved and first promising results from test reactors were presented, progress on the complex American stellarator concept was postponed until supercomputers enabled to build more advanced versions of this concept [13, 14, 15, 16].

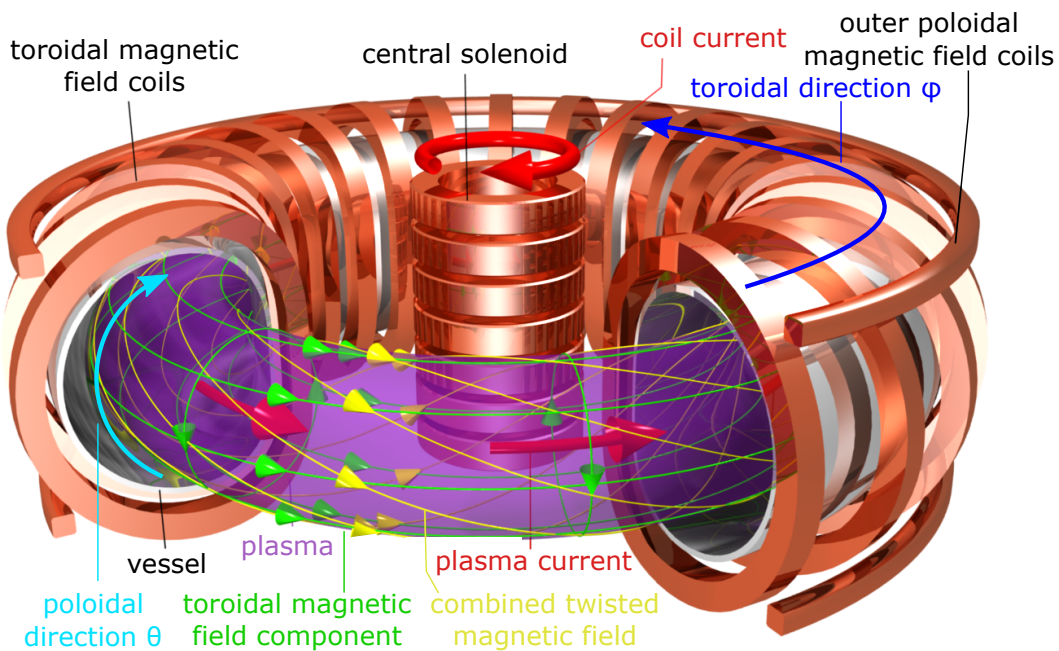


FIGURE 1.1: Structure of a tokamak as well as a definition of toroidal and poloidal directions [17].

As the acronym tokamak implies, it consists of a main vacuum chamber – in which the reaction materials are heated up to millions of degrees – and magnetic fields to confine the charged plasma particles. As illustrated in figure 1.1, the toroidal magnetic field is twisted to prevent charge separation, thus reduce particle drifts, which would degrade particle confinement [18, 19]. The toroidal component is created via the toroidal magnetic field coils, while the poloidal component is generated via a current driven inside the plasma. This current is induced by a central solenoid, hence a pulsed operation is one of the characteristic features of tokamaks. However, alternative current drive mechanisms can increase the pulse duration or might even enable a steady-state operation [20]. An important characteristic of nuclear fusion devices is the triple product $n \cdot T \cdot \tau_e$ with the plasma density n , temperature T and energy confinement time τ_e [19]. Hereby, τ_e is the characteristic time scale

of thermal energy loss expressed by $E_{\text{th}}/P_{\text{loss}}$. To reach ignition, the Lawson criterion [21] $nT\tau_e \geq 3 \cdot 10^{21}$ keVs/m³ has to be fulfilled. Ignition describes the values of the triple product, where the reaction becomes self-sustained, thus it is desirable for fusion power plants to reach this point. A major factor limiting the energy confinement time is the machine size. As τ_e increases with the size of the device, fusion power plants are foreseen to be large. ITER – with a fusion power gain of $Q \approx 10$ – will already have a major radius R_0 of 6.2 m [22]. The tokamak ASDEX Upgrade (AUG) is the successor of ASDEX (AxialSymmetrisches Divertor-EXperiment) and is located in Garching, Germany. It is a medium sized tokamak with a major radius of 1.65 m, with high heating power up to 27 MW [23]. It is equipped with a tungsten divertor and tungsten coated carbon tiles for the first wall. This was novel, as before AUG proved a full tungsten surface to be viable, mainly low- Z components (like carbon) were used [20, 24, 25]. An experimental run is referred to as discharge or shot and over 38000 had been realized since the first AUG discharge in 1991. The basic parameters of ASDEX Upgrade are shown in table 1.1.

TABLE 1.1: Basic parameters of ASDEX Upgrade [23]

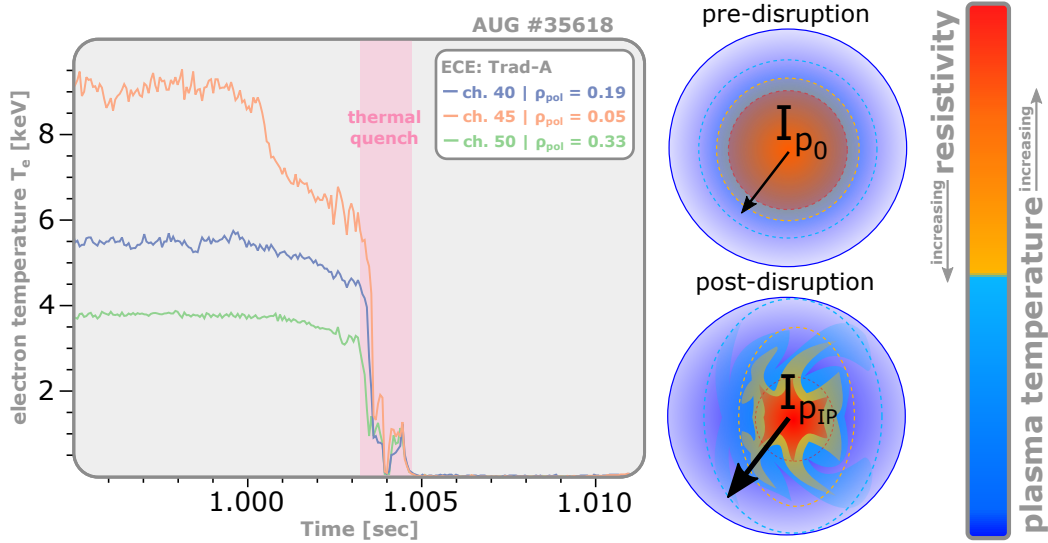
Parameter	Value
Major radius R_0	1.65 m
Minor radius a	0.5 m
Toroidal magnetic field B_t	≤ 3.1 T
Plasma current I_p	0.4 MA – 1.6 MA
Pulse duration	≤ 10 s
Electron density n_e	$\leq 2 \cdot 10^{20}$ m ⁻³
Heating power	≤ 27 MW
Energy confinement time τ_E	≤ 0.2 s

1.2 Disruptions and runaway electrons

To be able to obtain a stable and sustainable fusion process, the operational regime has to be carefully planned and active feedback control is necessary. Especially for the next generation of fusion devices such as ITER or DEMO, major disruptions are a significant threat [5, 6]. This section briefly explains disruptions and runaway electron generation based on chapter III of the ITER Physics Basis by T.C. Hender *et al.* [4].

In a tokamak device three main stability limits are present, namely the current, density and pressure limit. However, even within the limits of a stable

operational regime, major disruptions can also occur caused e.g. by a failure of technical components [26]. A major disruption might be compared to an interchange-like magneto-hydrodynamic instability at large scales, affecting the confined plasma and the periphery, which is illustrated in figure 1.2(b). Hereby, the inner, hotter plasma is exchanged and mixed with the colder plasma of the outer regions. During this process the plasma temperature drops from the keV to eV-range within $\sim 1 - 2$ ms. This is illustrated in figure 1.2(a) as the **thermal quench** (TQ) phase, the sudden drop in electron temperature (T_e) between 1.003 – 1.005 sec for ASDEX Upgrade discharge #35618.



(a) Sudden drop of the electron temperature during the **thermal quench** (in pink).

(b) Sketch of the breakup of good confinement during a disruption.

FIGURE 1.2: The quench phase of a disruption. In (a) the time evolution of the electron temperature for different flux surfaces are shown. This is illustrated by measurements of the electron cyclotron emission (ECE). The disruption is caused by massive gas injection, thus part of the signal drop-out might be caused by a density cut-off. In (b) a sketch of the events during the early quench phase is shown. As the profiles flatten with the breakup of good confinement, but flux conservation has to be maintained, the plasma current (I_p) initially increases leading to the IP-spike (see figure 1.3(a)). After this the current quench sets in and the plasma current drops rapidly. The plasma shape is adapted from simulations by Kleva *et. al.* [27].

In addition to the decrease in plasma temperature, the profiles also flatten rapidly. This is typically followed by a redistribution of the plasma current and flattening of the current profiles as well. The plasma temperature also heavily affects the conductance of the plasma $\sigma \propto T^{3/2}$, which is decreasing together with the plasma temperature. As the current profiles are flattening and conductance reduces, the plasma current has to increase to conserve the flux as illustrated in figure 1.2 and 1.3(a). This increase in plasma current (I_p) is referred to as **IP-spike** and depicted in figure 1.3(a). However, due

to Faraday’s law, the plasma current could not change on time scales this fast, thus the electric field inside the plasma increases significantly during the thermal quench via the relation $E = \eta \cdot J$ (Ohm’s law) as illustrated in figure 1.3(a) [8]. The IP-spike is followed by the exponential decay of the plasma current during the **current quench** (CQ), caused by the increased resistivity after the thermal quench. At some point, the position control of the plasma will ultimately fail with vanishing plasma current. However, the plasma current does not necessarily drop to zero within the CQ. The maximum of the collisional friction force acting on electrons is located around $p = m_e v_{th}$ with the thermal velocity of the electrons v_{th} . For electrons with higher momentum – such as supra-thermal electrons – the friction force decreases with increasing momentum [28]. Hence, high electric fields during the thermal quench can generate a beam of relativistic electrons. Electrons in the Maxwellian tail with momentum above the critical threshold p_{crit} get accelerated by the electric field but instead of increasing collisional friction, they experience less resistance for higher velocities, which ultimately leads to a runaway effect as depicted in figure 1.3(b) [8, 18, 28]. Therefore, these electrons are referred to as **runaway electrons**.

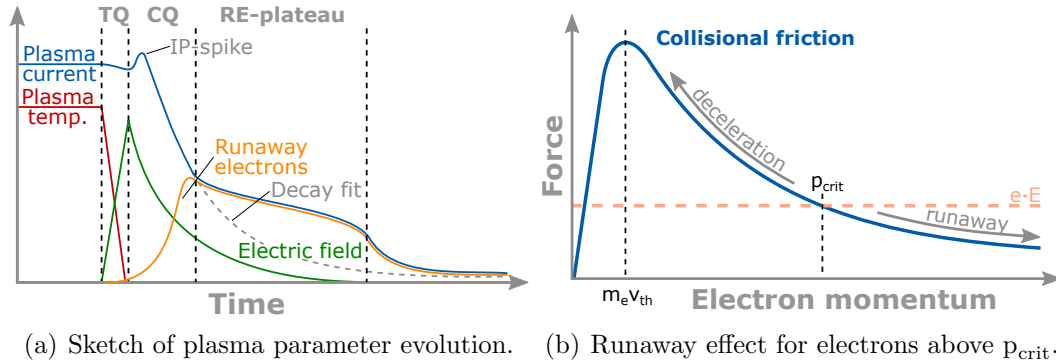


FIGURE 1.3: Runaway electron generation during disruptions. In (a) a sketch for the evolution of plasma parameters is provided [8]. In (b) the collisional friction is plotted against the electron energy to show the runaway effect [8, 18, 28].

Those so-called seed electrons can collide with electrons from the thermal bulk and transfer part of their energy to their collision partners. This is called avalanche effect as it exponentially increases the number of REs as long as a sufficiently strong electric field is present [8, 29]. The current held by the RE-beam can be in the range of several hundred kA, for large machines even in the MA range. This so-called runaway current can persist after the current quench. As the plasma current is almost entirely driven by REs now, this phase is referred to as **runaway plateau** (RE-plateau). If the confinement of this relativistic beam can not be sustained until the current had finally decayed, the electrons will hit the wall of the chamber, which can cause severe damage to the plasma facing components (PFC) [30]. For this reason active disruption mitigation and avoidance strategies are under development

to enable a safe operation. Examples for disruption mitigation techniques are shattered pellet injection (SPI) or **massive gas injection** (MGI). Hereby, impurities are injected into the plasma, radiating strongly. This reduces the localized heat loads onto the first wall (FW) during the disruption, as it distributes the loads over a larger surface area instead. For ITER a disruption mitigation system (DMS) is foreseen [5, 6]. However, mitigating the effects of disruptions alone is not necessarily enough, as the formation of strong RE-beams is also a major concern [4, 31]. Therefore, RE-suppression techniques are introduced in the following, based on the papers by Breizman *et al.* [28] and Pautasso *et al.* [32]. For a successful suppression of REs, the background electron density during the CQ should exceed a critical density n_c

$$n_c [10^{20} \text{ m}^{-3}] \approx 11 \cdot E_\phi [\text{V/m}] \quad (1.1)$$

estimated by the toroidal electric field E_ϕ . This field is caused by the decay of the plasma current during the CQ. Therefore, one RE-suppression technique is given by increasing the plasma density prior to the thermal quench via MGI or SPI, thus preventing the formation of REs in the first place. However, achieving the necessary electron densities in the plasma center on time, turns out to be challenging. Firstly, the disruption prediction has to be early enough, enabling the impurities to reach the plasma core. In addition, the injection speed is determined by the gas parameters (MGI) and ablation/ionization (SPI), respectively. Consequently, pre-disruption injection is a challenging task. Also the injected gas type has a large impact on the disruption behaviour. High-Z impurities provide larger amounts of electrons, while also possessing a larger collisional cross section ($\propto Z^2$) compared to low-Z impurities. On the other hand they lead to faster current quenches, thus higher toroidal electric fields, which increases the likelihood of a RE-plateau formation.

Another option is maintaining the plasma control and injecting impurities into the newly formed RE-plateau. This method does not prevent the formation of the RE-beam, but is aimed to increase RE-dissipation. This of course is accompanied by the risk of losing control early and the unmitigated RE-beam hitting the PFCs. For a massive injection of high-Z impurities into the RE-plateau, an increase in RE-dissipation had been observed [33, 34]. Injecting enough gas on time – without endangering the vacuum system – turned out to be very challenging.

Besides injecting impurities into the plasma, it is currently investigated whether driving certain modes inside the plasma unstable, is capable of mitigating the effects of REs or even suppressing their generation in the first place. A possible candidate for one of these modes is presented in more detail in section 1.2.2.

The analysis of this post-disruption mode in ASDEX is the central topic of this thesis.

1.2.1 Definition of the current quench

In this section I would like to provide the definition of the current quench used within the framework of this thesis. In figure 1.4(a) the plasma current evolution around the quench phase is displayed. At first it shows a slight reduction during the thermal quench as the plasma temperature decreases and with it the resistivity is increased [4]. This is followed by the IP-spike (see section 1.2). After the IP-spike one can observe a drop in plasma current, which is the actual **current quench**, followed by the runaway plateau.

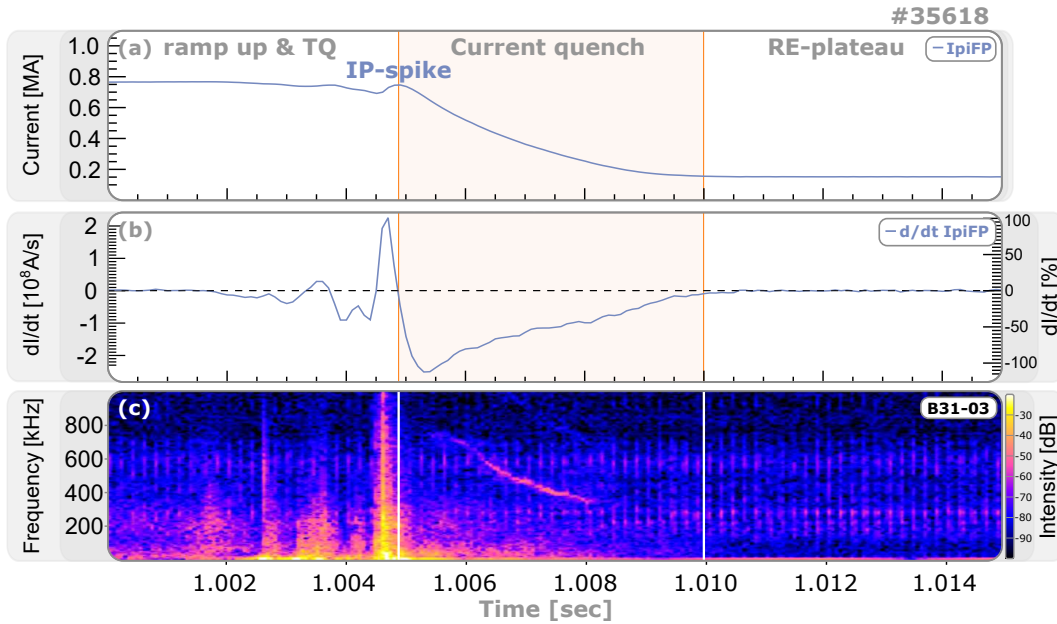


FIGURE 1.4: Definition of the CQ time window. In (a) the evolution of the plasma current is given, with its time derivative depicted in (b). In (c) a spectrogram for the magnetic coil B31-03 is provided, which shows the presence of a sweeping mode.

In figure 1.4(b) the time derivative of the plasma current dI/dt is shown. With the IP-spike our definition of the current quench starts and it expands until the change in plasma current approaches zero again. As the consecutive RE-plateau also shows a slight decay over time, a threshold is necessary to determine a reasonable end point of the current quench. I normalized the time derivative of the current with its maximum. The zero crossing of the derivative is chosen as the start point of the CQ, which is equal to the maximum of the IP-spike. As a threshold to determine the end point, I set -0.25%. In addition the algorithm checks whether the derivative approaches zero or a random fluctuation occurred, by taking the subsequent evolution of the derivative into account. In figure 1.4 the definition from above is highlighted in orange. Figure 1.4(c) shows the spectrogram for the magnetic coil B31-03, which shows the presence of a mode chirping from about 800 to 400 kHz.

1.2.2 Post-disruption mode

Modes like the one shown in figure 1.4(c) have been observed in almost all disruptions created to study RE-generation in ASDEX Upgrade. They have also been observed in natural disruptions, while their origin is still unknown.

Recent experiments in DIII-D

Post-disruption modes were observed also in the tokamak DIII-D. While a wide range of modes at different frequencies had been observed in DIII-D, I want to focus on the type of mode presented in the paper by Lvovskiy *et al.* [7]. Consequently, this paper is used as the basis for this section, investigating the effect of instabilities on the RE-current formation.

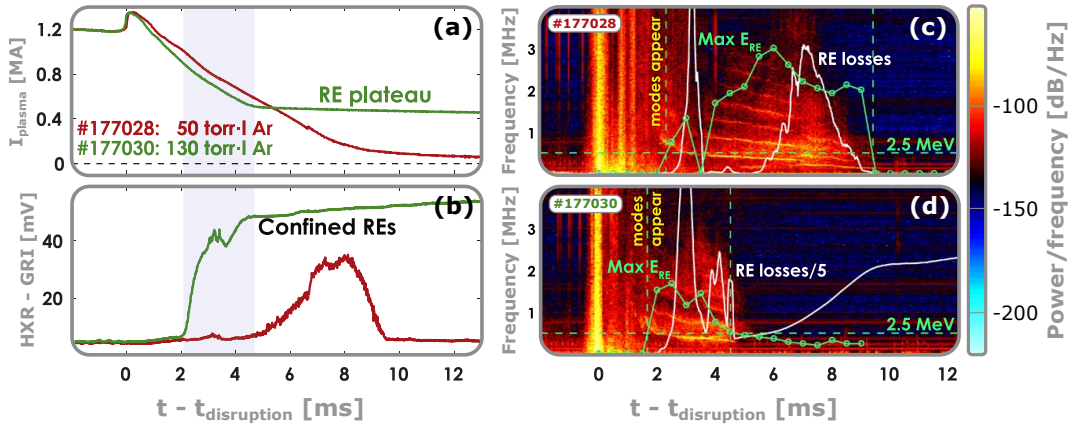


FIGURE 1.5: Experimental results from DIII-D with plots taken from Lvovskiy *et al.* [7]. In (a) the plasma current evolution is shown. The amount of confined REs is indicated by the hard X-ray measurement in (b). The spectrograms for the discharges #177028 and #177030 are given in (c) and (d), respectively.

In figure 1.5 two discharges are depicted with different amount of argon injected via MGI. Both discharges show the presence of post-disruption modes as shown in figure 1.5(c, d). However, for the discharge with less argon injected (c) the length of these modes and the number of upper harmonics is increased with respect to the discharge with more argon injected (d). At the same time also the length of the current quench is increased and the subsequent RE-current is decreased significantly for the lower argon case as shown in figure 1.5(a). In 1.5(b) the amount of runaway electrons is indicated via the hard X-ray (HXR) emissions of the gamma ray imager (GRI) diagnostic [35]. This plot shows a faster and higher build-up of the RE-plateau in the case of higher argon injection. The investigations on the RE-plateau formation lead to the mechanism proposed by Lvovskiy *et al.* in figure 1.6. Hereby, smaller amounts of argon during MGIs and/or larger plasma currents lead to increased integrated loop voltages (U_{loop}) and population of high-energy runaway electrons. This large population is proposed to increase instabilities, which could

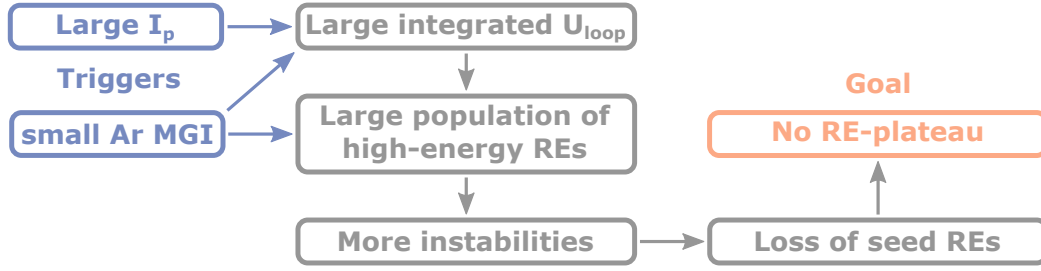


FIGURE 1.6: Proposed mechanism behind RE-plateau suppression adapted from Lvovskiy *et al.* [7]. Hereby, small argon MGIs as well as large plasma currents are supposed to suppress the RE-plateau.

lead to a loss of seed REs and ultimately prevent the formation of a RE-plateau due to the avalanche effect. The instabilities should be therefore visible as the **post-disruption modes** as proposed by Lvovskiy *et al.* [7].

In the contribution by Chang Liu *et al.* [9], these instabilities are proposed to be **compressional Alfvén eigenmodes** (CAEs) driven by runaway electrons.

Post-disruption mode investigations for ASDEX Upgrade

In the present thesis I want to provide another potential driving mechanism – **global Alfvén eigenmodes** (GAEs) – which match the experimental observations in ASDEX Upgrade. The magnetic measurements for AUG used in the scope of this thesis, allow to observe frequencies up to 1 MHz. Consequently, only the lowest of the harmonics displayed in figure 1.5(c, d) would be visible. This harmonic will be characterized in detail in section 4.1. A detailed analysis of potential effects by these modes on the subsequent RE-plateau for AUG and a comparison to the results from DIII-D will be presented in section 5.3.3.

For a better understanding of the proposed driving mechanisms, Alfvén waves are introduced in the following section.

1.3 Alfvén waves

The following section is based on chapter 4.4.3 in the textbook by Stroth [18]. As Hannes Alfvén proposed in *Nature* in 1942 [36], electromagnetic waves can propagate in magnetized plasmas. They can be classified into shear and compressional Alfvén waves. The **shear Alfvén wave** (SAW) propagates in parallel direction with respect to the background magnetic field \vec{B}_0 and has a perpendicular displacement vector $\vec{\xi}_0$ ($\vec{k} \parallel \vec{B}_0 \perp \vec{\xi}$) as depicted in figure 1.7(a). The propagation velocity is given by the **Alfvén velocity**

$$v_A = \frac{B_0}{\sqrt{\mu_0 \rho_m}} \quad (1.2)$$

with the mass density of charged particles $\rho_m = \sum_s n_s \cdot m_s$ for each particle species (s). Like electromagnetic waves in the vacuum, the perturbation of the magnetic field is also perpendicular to an induced electric field in a plasma. This field drives a polarization current, which closes the current loop in parallel direction with respect to the magnetic field, due to the quasi-neutrality of the plasma. The restoring force, which also drives the propagation of this wave is given by the magnetic tension of field lines – which can be compared to the behaviour of a guitar string. As only the Alfvén velocity contributes to the propagation velocity, this wave is also referred to as the **slow Alfvén wave**.

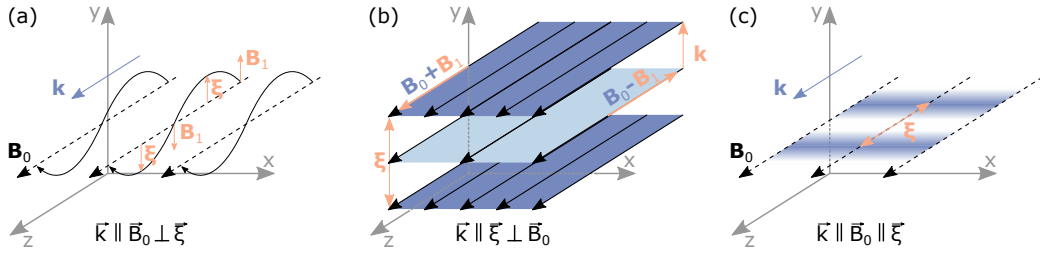


FIGURE 1.7: Sketches for the shear (a) and compressional (b) Alfvén wave as well as the sound wave (c). The images are adapted from the textbook by Stroth [18].

In contrast, the propagation velocity for **compressional Alfvén waves** depends also on the sound velocity c_s and is given by

$$v = \sqrt{v_A^2 + c_s^2}, \quad (1.3)$$

thus it is also called the **fast Alfvén wave**. Its propagation direction is perpendicular to \vec{B}_0 and parallel to the displacement vector ($\vec{k} \parallel \vec{\xi} \perp \vec{B}_0$) as shown in figure 1.7(b). As a result the magnetic perturbation \vec{B}_1 – which is parallel to \vec{B}_0 – alternately increases and decreases the total magnetic field, as the wave travels across the flux surfaces, indicated by the shaded areas in figure 1.7(b). For this Alfvén wave, the magnetic pressure is contributing to the restoring force. In case of $\vec{k} \parallel \vec{\xi} \parallel \vec{B}_0$ we observe a sound wave, illustrated in figure 1.7(c). The (ion) sound velocity is given by the relation

$$c_s = \frac{\omega}{k} = \sqrt{\frac{\gamma p_0}{\rho_{m0}}} \approx \sqrt{\frac{T_e + \gamma_i T_i}{m_i}} \quad (1.4)$$

with the unperturbed plasma pressure p_0 and mass density ρ_{m0} , the adiabatic coefficient of the ions γ_i as well as electron/ion temperature $T_{e/i}$ in eV. The examples presented in figure 1.7 illustrate purely parallel or perpendicular vector quantities; however, in reality one also encounters waves inside a plasma, which possess both components and show a mixture of these behaviours.

1.3.1 Alfvén eigenmodes in a tokamak environment

Alfvén waves frequently occur in magnetically confined plasmas. Here the plasma geometry and parameters affect the behaviour of Alfvén waves, which leads to excitation of Alfvén eigenmodes. This section is based on the papers of Lauber [37] and Heidbrink [38].

The Alfvén continuum

For shear Alfvén waves with frequency ω being small compared to the ion cyclotron frequency Ω_i , one can neglect kinetic effects and the dispersion relation is expressed by

$$\omega = k_{\parallel} \cdot v_A. \quad (1.5)$$

Due to periodicity constraints in the tokamak environment, the parallel wave number has to fulfil the condition $k_{\parallel} = [n - m/q(r)]/R$. Hereby,

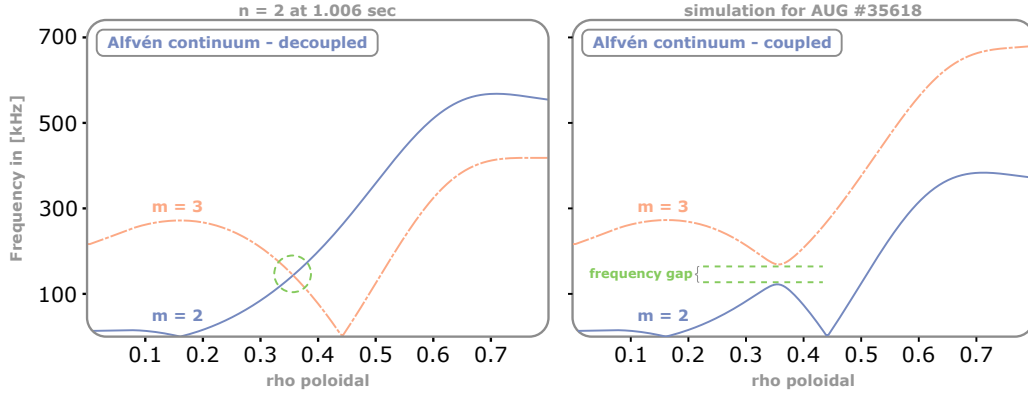
$$q(r) = \frac{r \cdot B_{\text{tor}}}{R \cdot B_{\text{pol}}} \quad (1.6)$$

is the safety factor, R the major radius, while n and m are the toroidal and poloidal mode numbers, respectively. Inserting this condition of the parallel wave number into the dispersion relation from equation (1.5) yields

$$\omega^2 = k_{\parallel}^2 \cdot v_A^2 = \left(\frac{n - m/q(r)}{R} \right)^2 \cdot \frac{B(r)^2}{\mu_0 m_i n(r)} \quad (1.7)$$

which is now a function of radius. Waves satisfying this condition define the **Alfvén continuum**. As already indicated by the first term in equation (1.7), the shear Alfvén continuum is composed of different branches for each mode number. As examples, the $m = 2$ and $m = 3$ branches are plotted in figure 1.8(a). For this simple decomposition, every SAW with a fixed frequency will have at least one intersection with a continuum line.

Let us consider a wave packet with the finite frequency width $\Delta\omega$ and radial extent. If the wave packet reaches one of the resonant layers, represented by the continuum lines in figure 1.8(a), phase mixing will occur. As the dispersion relation is a function of radius, the wave package will be sheared and ultimately



(a) Decoupled Alfvén continuum for poloidal mode numbers $m = 2$ and $m = 3$, respectively. (b) Periodic variations of v_A generate frequency gaps in the Alfvén continuum.

FIGURE 1.8: Effect of mode coupling in the Alfvén continuum. The continuum lines were calculated with LIGKA [39, 40] simulations for the discharge #35618.

disperse, illustrated in figure 1.9. This results in a strong damping effect at the resonant layers of the continuum, for which the damping rate γ is proportional to the phase velocity gradient $\gamma \propto d\omega/dr$.

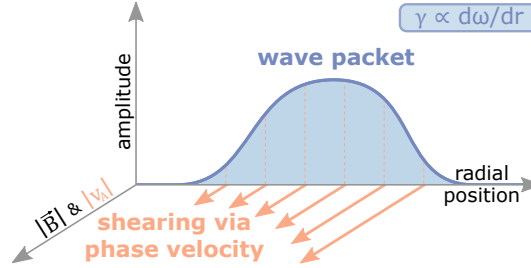
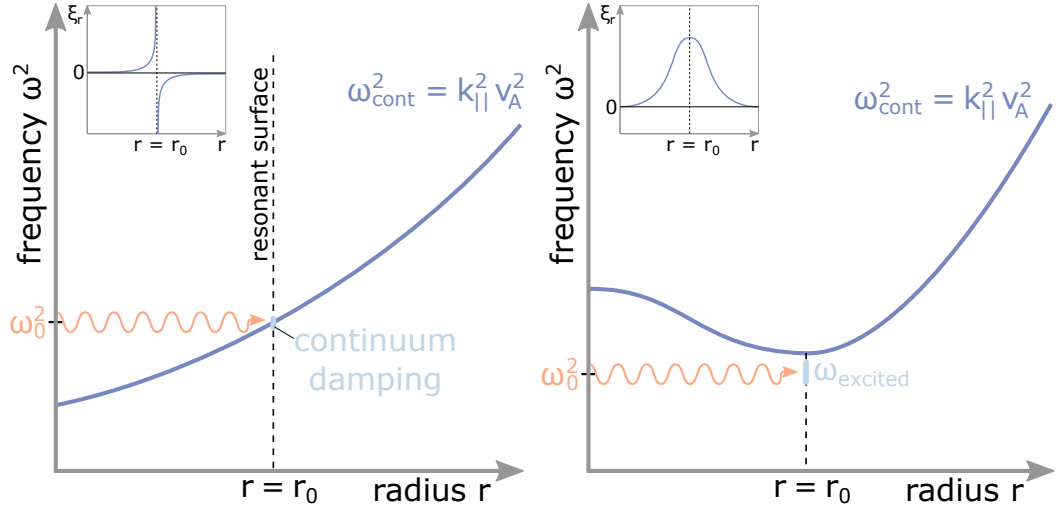
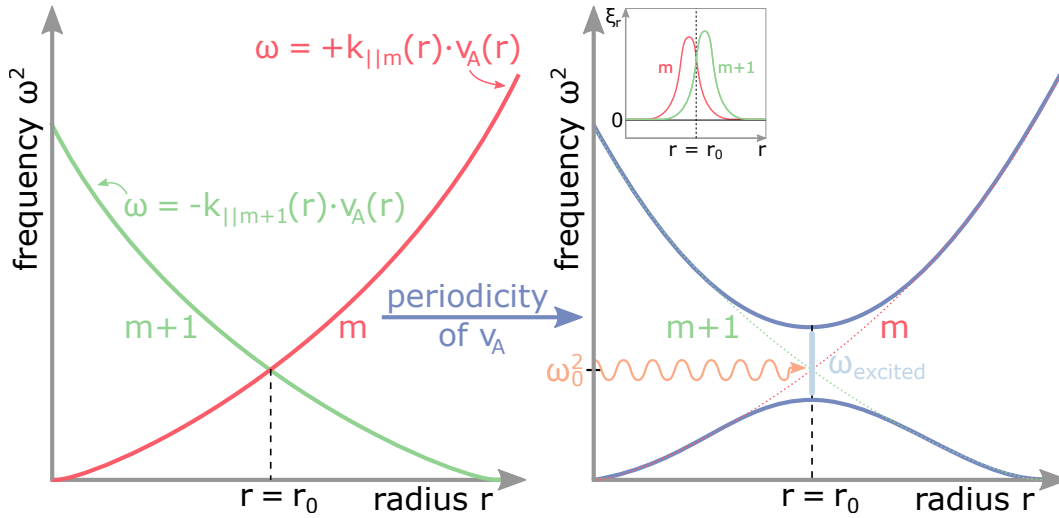


FIGURE 1.9: Sketch of the continuum damping. The magnetic field strength and consequently the Alfvén velocity are functions of radius. Therefore, the wave packet with a finite radial extent is sheared in the velocity field. The damping rate γ is proportional to $d\omega/dr$. The image is adapted from the work of Heidbrink [38].

Therefore, this phenomenon is referred to as **continuum damping**. Consequently, one would expect no modes – or at least no discrete modes with small spectral width – to appear in this setup as the typical driving mechanisms can not provide enough energy. However, gaps in the Alfvén continuum are present illustrated in figure 1.8(b), which allow global modes to exist. These gaps are caused by periodic variations of the Alfvén velocity along the field lines, similar to the existence of the electron band gap in conductors, due to the periodicity of the lattice. As any periodic variation of v_A can enable the generation of gaps, a wide range of plasma parameters can lead to Alfvénic activity inside the plasma. One can therefore classify a mode depending on the type of symmetry breaking. Figure 1.10 shows three types of modes excited by an antenna, together with their respective mode structure in the upper



(a) Radio frequency (RF) wave hits the Alfvén continuum. The excitation quickly disperses, due to continuum damping. (b) **Extremum type:** Excitation of a wave close to the extremum with a single mode number. Examples are reverse shear Alfvén eigenmodes (RSAEs) and global Alfvén eigenmodes (GAEs).



(c) **Coupling type:** Modes can be excited in the Alfvén continuum gap. It is caused by the coupling of neighbouring branches due to periodicity of v_A , thus the mode structure shows the two components m and $m + 1$, respectively. Examples are toroidal Alfvén eigenmodes (TAEs).

FIGURE 1.10: Adapted from the original contribution by Pinches [41] and its adaption by Heidbrink [38]. The plots illustrates external excitations of waves by an antenna. In the upper-left corners, the mode structures is depicted.

left corner. While modes at the continuum (a) quickly disperse, modes inside the frequency gaps (b) and (c) can survive. Figure 1.10(b) represents the **extremum type**. Hereby, modes are excited close to the extremum (typically a minimum), while a single poloidal mode number is prominent. On the other hand the origin of coupling type modes is given by the interaction of poloidal harmonics, as shown in figure 1.10(c). In fusion experiments, different kinds of symmetry breaking mechanisms are present. Parameters, which describe the plasma shape – like ellipticity or triangularity – can generate gaps in the continuum. A prominent example is the toroidal Alfvén eigenmode (TAE), where gaps are generated by toroidicity of the plasma. Additionally, already the arrangement of the field coils at discrete positions itself generates ripples in the magnetic field strength and cause periodic variations of v_A .

1.3.2 Global Alfvén eigenmodes (GAEs)

An example for gap modes is the global Alfvén eigenmode [42]. It is classified as a extremum type mode as shown in figure 1.10(b), thus only shows a single poloidal harmonic. For typical experimental setups, this extremum is most likely a minimum in the Alfvén continuum [38, 42]. This is due to higher peaked plasma current profiles compared to density profiles for present day tokamaks [42]. Therefore, GAEs are expected just below the the minima in the Alfvén continuum for typical scenarios [38, 42]. However, during disruptions – especially during ones mitigated via impurity injection – the plasma profiles vary significantly. This also affects the q -profile, consequently the Alfvén velocity and continuum. Higher plasma densities towards the edge region, can also lead to the formation of a maximum in the continuum. GAEs are expected to be present slightly above this maximum for these cases, which will be discussed in section 6.2 in more detail. As stated in the paper by Chang Liu *et al.* [9], GAEs were proposed as a promising candidate for the post-disruption modes. While they focused on compressional Alfvén eigenmodes (CAEs) in their work, we provide a mode driving mechanism based on GAEs in section 6.2. In this frequency range, only GAEs or elliptical Alfvén eigenmodes (EAEs) are expected. However, as shown in section 2.3, the experiments use circular plasmas, thus EAEs should not appear.

1.3.3 Compressional Alfvén eigenmodes (CAEs)

Besides the SAW, also compressional Alfvén eigenmodes can be observed in fusion experiments. For low aspect ratio tokamaks, CAEs are expected to be localized in the outboard midplane region close to the plasma edge, due to a potential well [43, 44, 45]. Also damping rates are significantly reduced, if the wave frequency is a low multiple of the edge thermal ion cyclotron frequency [44]. Evidence for the outer midplane localization was found by Fredrickson *et al.* in a comparison between simulation and experiment at the National Spherical Torus Experiment (NSTX) [45].

1.4 Fourier transformations and spectrograms

To be able to investigate the complex time-frequency evolution of these modes inside the plasma, **spectrograms** are important tools. They are based on transformations, formulated by Jean Baptiste Joseph Fourier in 1822 [46]. Fourier transformations are used to extract the different frequency components of a signal and illustrate them via a spectral representation [47]. One method to represent the frequency evolution of a signal are spectrograms, which are based on short time Fourier transformations (STFTs) [47]. The transformation

$$Sf(u, \xi) = \langle f, g_{u, \xi} \rangle = \int_{-\infty}^{+\infty} f(t)g(t-u)e^{-i\xi t} dt \quad (1.8)$$

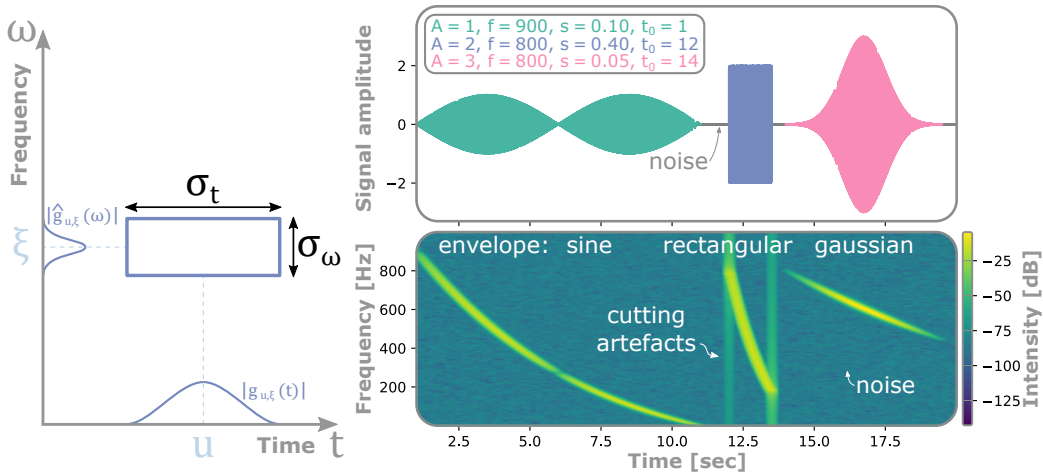
is localized in time around $t = u$ due to the real and symmetric window function $g(t)$ which transforms under Fourier transformations as [47]

$$g_{u, \xi}(t) = e^{i\xi t}g(t-u). \quad (1.9)$$

This concept was introduced by Dennis Gabor in 1946 to study frequency variations of sound waves [47, 48]. Based on the STFT in (1.8) a spectrogram (P_S) is defined by

$$P_S f(u, \xi) = |Sf(u, \xi)|^2 = \left| \int_{-\infty}^{+\infty} f(t)g(t-u)e^{-i\xi t} dt \right|^2 \quad (1.10)$$

the **energy density** of the signal [47]. However, due to information conservation, a signal sampled with N data points can not provide a two dimensional $N \times N$ representation with the same information density. This leads to a similar phenomenon as observed for the uncertainty principle in quantum physics.



(a) Heisenberg box concept. (b) Spectrograms for test signals with different enveloping functions and $a(t) = A \cdot \sin 2\pi \cdot f \cdot e^{-s \cdot (t-t_0)} \cdot (t-t_0)$. Adapted from Mallat [47].

FIGURE 1.11: In (a) the concept of Heisenberg boxes is illustrated. In (b) a spectrogram for test signals with different enveloping functions (sine/rect./gaussian) is given.

The time- and frequency domains are not independent, thus the resolution in both domains is linked. This can be illustrated by a Heisenberg box (see figure 1.11(a)) with a time and frequency width σ_t and σ_f , respectively [47]. Hereby, the relation $\sigma_t \cdot \sigma_f \geq 1/2$ has to be fulfilled. Therefore, the number of FFTs as well as the window function affect the spectrogram. This time-frequency-quantization enables to resolve the time-frequency evolution of signals and is therefore a central tool for the mode analysis in this thesis. For generating spectrograms, certain window functions are used, each with individual characteristics. They are necessary, since slicing signals via a step-like function introduces strong artefacts. To represent sharp edges in the signal – for example by discontinuities – multiple harmonics are needed. This is visible as a broad frequency band within the spectrogram, which extends from low to high frequencies as shown in figure 1.11(b). Window functions reduce this effect, as they do not cut the signal, but provide a continuous opening of the filter. Without a window function, spectrograms would show these artifacts at the boundary of every time interval. Most frequently the **Gaussian-** or **Hann-**windows are applied due to their properties.

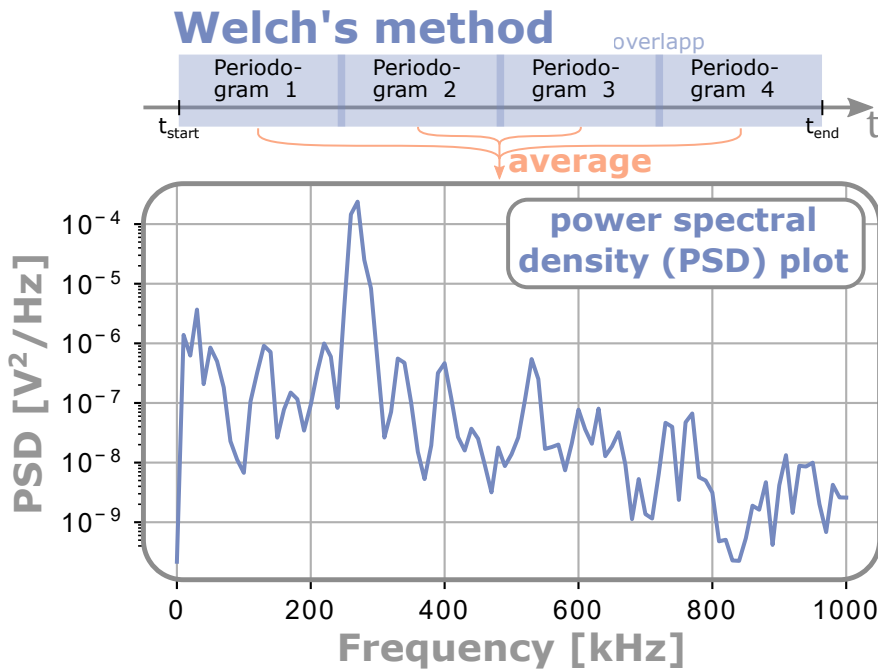


FIGURE 1.12: Welch's method is illustrated as well as the power spectral density plot (PSD) given. It is calculated by averaging over multiple periodograms generated for subdivided time intervals of a signal.

Another representation for the frequency composition of signals is a 2D **power spectral density** (PSD) plot as given in 1.12. Here the PSD is plotted against the frequency, thus the main frequency components are visible as prominent peaks. For this thesis, I work with **Welch's method** [49]. This algorithm splits the signal into smaller time segments and averages over periodograms, created for each interval, to obtain the PSD estimate.

Chapter 2

Experimental Setup

In this chapter the main diagnostics within the thesis work and the experimental setup for RE-generating disruptions are presented. In section 2.1 the magnetic pick-up coil system of ASDEX-Upgrade is displayed. The Soft X-ray diagnostic is explained in section 2.2 and the setup for the experiments on the post-disruption modes is presented in section 2.3.

2.1 In-vessel magnetic pick-up coils

ASDEX-Upgrade is equipped with multiple sets of magnetic pick-up coils to measure fluctuations in the magnetic signals. Changes in the magnetic field induce a current inside these coils. The true amplitude of a specific oscillation is proportional to its time derivative $\hat{B}_\alpha \propto d/dt \hat{B}_\alpha / f$. Hereby, f is the frequency of the oscillation and α represents the radial (r) or poloidal (θ) component of the magnetic field, respectively [50]. The magnetic measurements in fusion devices such as ASDEX-Upgrade are frequently used to examine phenomenon inside the confined region as well as the scrape-off layer (SOL). **Ballooning**-coils (BAL-coils) measuring the radial magnetic field B_r , are often used to investigate ballooning modes, hence given their name. The poloidal magnetic field B_θ is measured by Mirnov-coils [51]. Alfvén waves, introduced in section 1.3, cause local perturbations of the magnetic field, therefore the effect of these waves is visible within the magnetic measurements. Mode structure analysis is made possible through a large number of coils distributed inside the vessel [52]. This variety of applications makes the magnetic measurements a powerful tool and contributes to its frequent use. Figure 2.1 shows the position of selected coils in a toroidal and poloidal cross section of the vacuum vessel, respectively. The data is acquired via the HotLink solution, which allows to obtain a sampling rate up to 2 MHz [53].

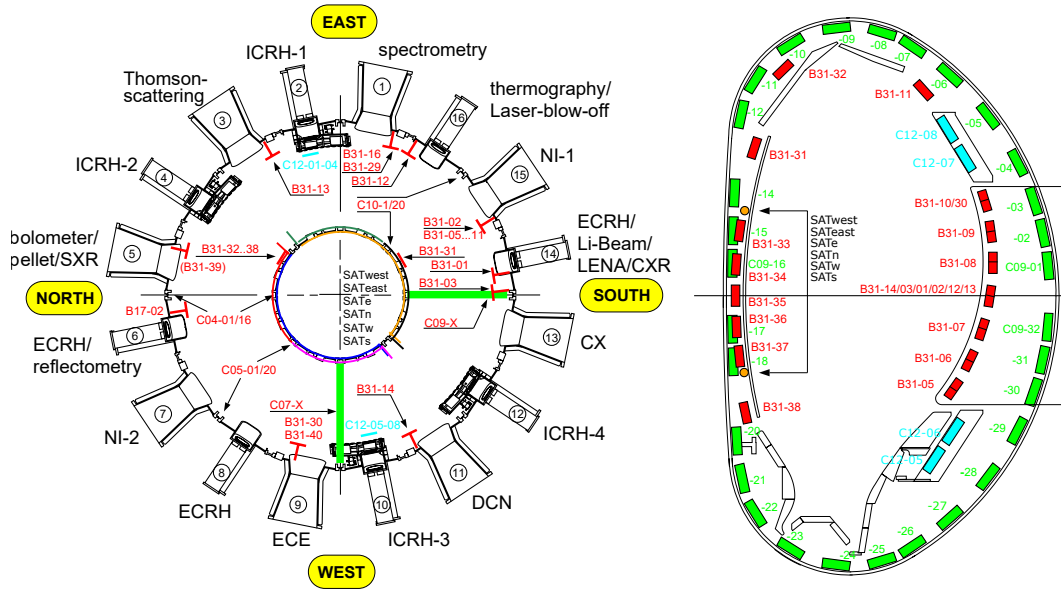


FIGURE 2.1: The toroidal (left) and poloidal (right) cross section of the vacuum vessel of AUG including the magnetic coils [53]. The **Mirnov**- (green) and **BAL**-coils (red) were examined in more detail.

2.2 Soft X-ray measurements

The Soft X-ray (SXR) diagnostic measures a specific range of the radiation power density or emissivity of the plasma [50]. Sources for the SXR emissions are bremsstrahlung, recombination- and line radiation, respectively [54]. Consequently, the emissivity of a plasma in the SXR range depends on the electron and impurity densities as well as the electron temperature [50]. While the emitted radiation is proportional to $Z_{\text{eff}} n^2 \sqrt{T}$ [55], the measurements are proportional to $Z_{\text{eff}} n^2 T$ due to the filters applied to the cameras [54]. SXR measurements are line integrated, influenced by a variety of different factors and the emissivity is not necessarily constant on a flux surface, thus interpreting the results is highly complex [50]. In AUG a SXR-camera consists of one to three diode arrays as shown in figure 2.2. A sketch for one of these heads is shown in figure 2.3. The SXR detectors include a 75 μm thin beryllium filter to suppress low energy photons [50, 54]. Due to the pinhole geometry depicted in figure 2.3 and chips in use, multiple lines of sight (LOSs) per diode array can be processed simultaneously. 15 probe heads (figure 2.3) are used and over 200 LOSs create a narrow poloidal grid [54]. 128 of the channels are so-called fast SXR-channels with a sampling rate of 2 MHz, while the other 80 are referred to as slow SXR-channels with a sampling rate of 0.5 MHz [54]. In figure 2.4 the LOSs of the SXR diagnostic in AUG are displayed. The cameras are located in sector 11 except for camera F, which shares the same poloidal angles with camera G, but is located at a different toroidal position (sector 5).

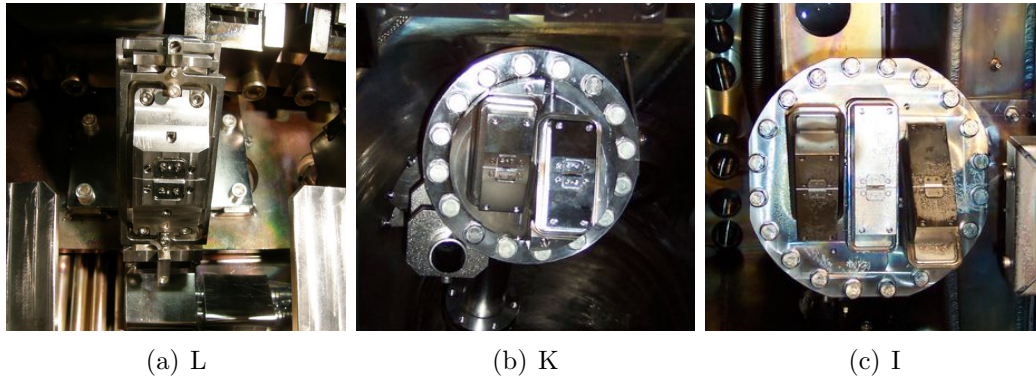


FIGURE 2.2: Examples for SXR-cameras with different number of probe heads [54]. Each of these probe heads contains an array of diodes (see figure 2.3) and creates individual LOSs.

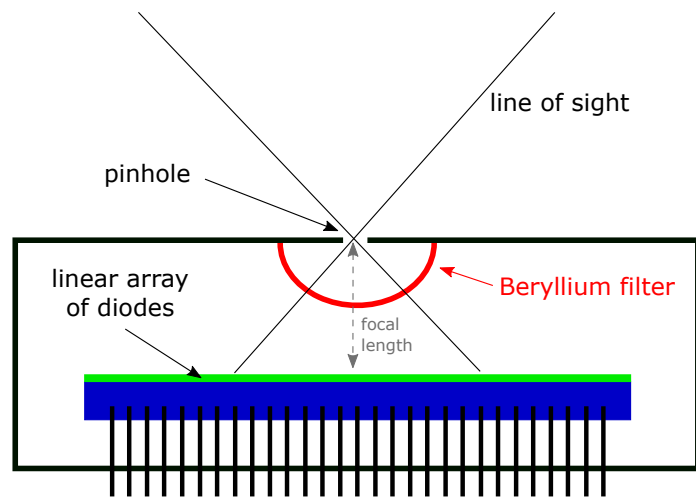


FIGURE 2.3: Sketch of a pinhole probe head for the SXR-cameras [54]. The geometry in combination with the intersected chip, splits the field of view into several distinct LOSs. The filter (typically 75 μm Beryllium) suppresses low energetic photons.

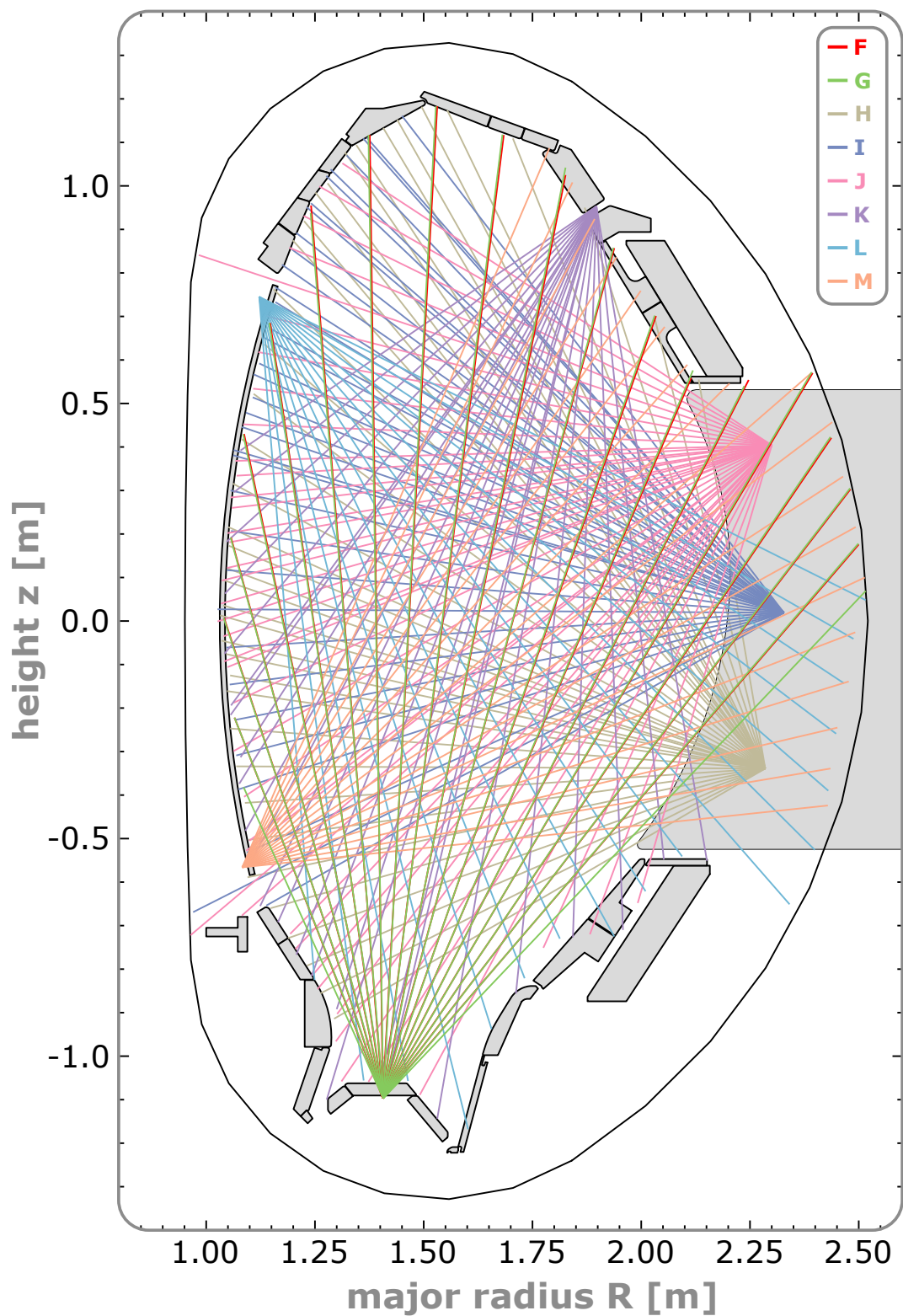


FIGURE 2.4: Poloidal cross section of the AUG vacuum chamber with LOSs of the SXR diagnostic. The LOSs for each of the cameras F – M are displayed in the same color. Camera F and G share the same poloidal angles but are located at different toroidal positions. The plot has been created on the data provided by the internal diaggeom tool.

2.3 Setup for the experiments on the post-disruption modes

The database for this thesis consists of 180 discharges with the primary goal of runaway electron generation. The database ranges from shot number #31318 (July 2014) to #38088 (July 2020). The discharges are all inner wall limited (IWL), circular plasmas (elongation $\kappa \approx 1.1$). This configuration was chosen, as the formation of a RE-plateau is more likely for circular flux surfaces compared to elongated plasmas. This is mostly due to an increased vertical stability of circular plasmas [32] and also a minor contribution of the flux surface configuration [28]. An excerpt of global parameters for these discharges is shown in table 2.1.

TABLE 2.1: Global parameter ranges for the discharges in the database. In the left column the parameters and their [units] are given. On the right the parameter ranges are shown. The numbers inside the brackets represent the number of discharges within this parameter range, with a total of 180.

GLOBAL PARAMETER RANGES				
B_t [T]	< 2.45 (17)	2.45 – 2.55 (151)	2.7 – 2.9 (12)	
I_p [MA]	< 0.75 (15)	0.75 – 0.85 (149)	0.85 – 1.17 (16)	
n_{pre} [m^{-3}]	around the target density of $3 \cdot 10^{19} \text{ m}^{-3}$			
q_{95}	< 3.7 (27)	3.7 – 4.05 (151)	4.22 & 6.01 (2)	
P_{ECRH} [MW]	0 (40)	< 2.0 (63)	2.0 – 2.6 (100)	> 2.6 (17)
MGI gas type	Ar (166)	Ne (3)	Kr (5)	Ar + D ₂ (6)

The experiments consist of three phases, illustrated in figure 2.5. The first phase is referred to as the current ramp-up phase. During the first second of the discharge the plasma current (I_p) is ramped up to values typically around 800 kA and the target density (pre-disruption plasma density n_{pre}) is around $3 \cdot 10^{19} \text{ m}^{-3}$. At $t = 1 \text{ s}$, a valve is triggered and the massive gas injection takes place, which leads to the desired disruption. As shown in table 2.1 the main MGI gas type was argon with 166 out of 180 discharges. Typical argon quantities injected into the plasma during MGIs are between $3 \cdot 10^{20}$ to $4.8 \cdot 10^{21}$ atoms. The gas penetrates the plasma and starts to radiate away the previously confined energy [56].

Within few milliseconds the plasma cools down from around 10 keV to a few eV and the plasma current collapses. This defines the quench phase discussed in more detail in sections 1.2 and 1.2.1.

As the experiments were designed to investigate runaway electron generation [32, 34], the last phase of the discharges is mostly characterized by the presence of a RE-plateau. Therefore, $\sim 77\%$ of the discharges show a runaway

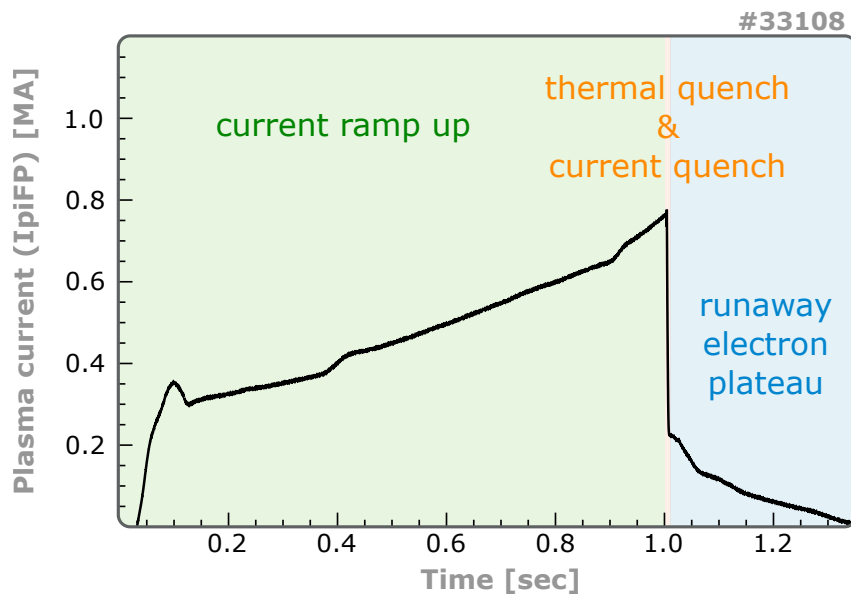


FIGURE 2.5: Three phases of the experiments on runaway electron generation and post-disruption modes: At first the current ramp-up phase is shown (green), followed by the quench phase (orange) and the subsequent RE-plateau (blue).

current above 50 kA. For decreasing plasma current, the stability and position control becomes increasingly difficult. A more detailed description of the execution of experiments is given in the papers by Pautasso *et al.* [32, 34].

Chapter 3

Mode analysis methods

During my thesis work, I implemented special tools to enable the analysis of the post disruption modes. The central component of the analysis is the mode-tracing, which uses Dijkstra’s algorithm.

At first, Dijkstra’s algorithm is explained in section 3.1 with the help of a calculation example. In section 3.2 the mode tracing algorithm is presented in detail, which includes the implementation process and features available within this tool set. Finally section 3.3 covers a tool to investigate amplitudes within the Soft X-ray LOSs.

3.1 Dijkstra’s algorithm

The mode tracing algorithm implemented is based on Dijkstra’s algorithm [57]. This algorithm was published by Edsger W. Dijkstra in 1959. It takes a set of nodes, the start and desired end point as well as the cost to transit between them and will find the path with the globally lowest cost possible to reach the destination. The algorithm is explained with help of the following example.

Our map consists of the nodes A to E (with start A and end E) displayed in figure 3.1. The distance or ”cost” between connected nodes is known (either as direct input data or from a **cost function**). Initially we set the connections between the nodes to infinity (figure 3.1(a)). We start the algorithm with our starting node A. In figure 3.1 the node under investigation is highlighted in red. We now check the distance from A to B with the help of the provided cost function. The cost between A and B is given as 5 (figure 3.1(b)). We update element $A \rightarrow B$ in our sorted list to the value 5 (figure 3.1(c)). In addition we add a side note for B, that the path with the currently lowest cost to reach B, is over A, thus A is its parent node. This side note – indicated by the subscripts in figure 3.1 – is created for each node in our grid and will help to keep track of the shortest path. The next connection to evaluate and update in the list is $A \rightarrow C$ with the value 25. Now all paths connected to A are evaluated, thus we finished to examine this node. In figure 3.1(d) this is indicated by changing the node’s color to dark gray. The next node in our

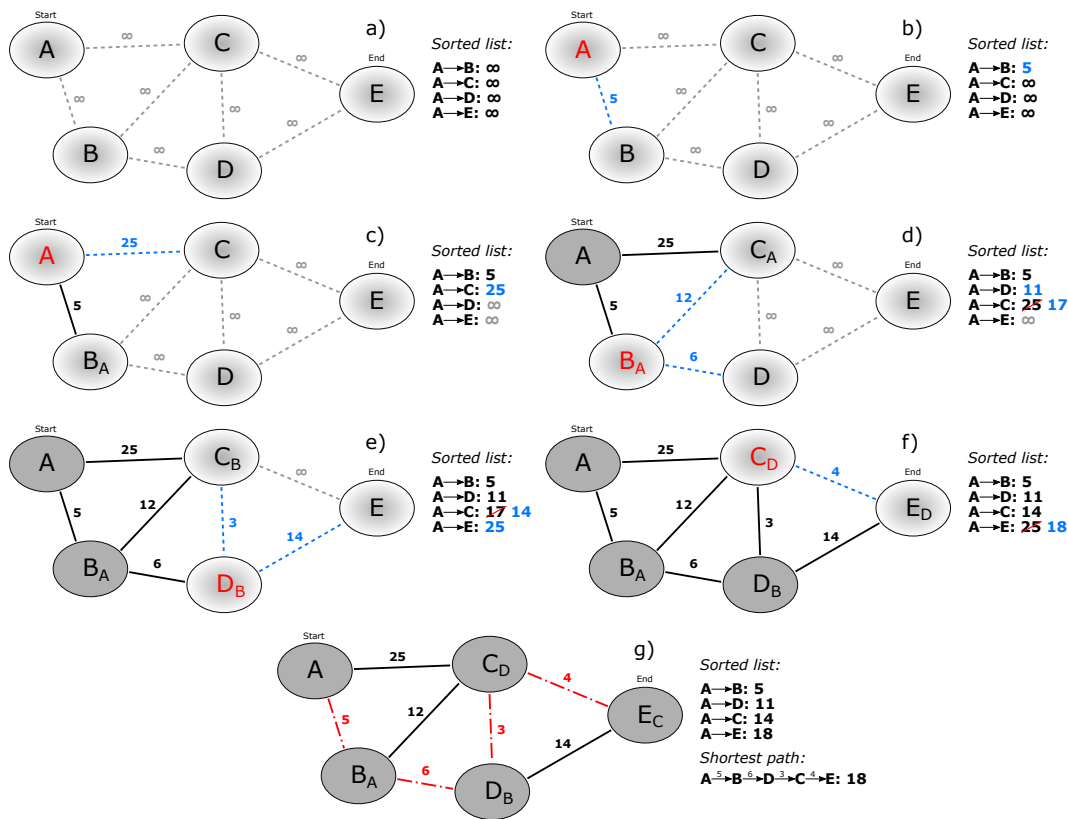


FIGURE 3.1: Sketch for an example of Dijkstra's algorithm. It shows the grid points A – E with starting point A and destination E. A detailed explanation of each step is given in the text.

sorted list with the lowest costs to reach is B, therefore we continue with this one. We again check both paths connected to B, which yields $B \rightarrow C : 12$ and $B \rightarrow D : 6$ respectively. We update the cost for $A \rightarrow C : 25$ 17 – as the shortest connection is given by $A \rightarrow B \rightarrow C$ – and also the parent node for C is now B (figure 3.1(e)). In addition we determined $A \rightarrow D : 11$ as the next shortest path, therefore continue with node D.

This routine – checking all paths connected to the node of interest and updating the sorted list – is repeated until all nodes were examined or the next node on the sorted list to examine is our destination. With the help of our side notes we determine the path with the globally lowest cost. In our example we wanted to investigate the shortest path from start A to E. Therefore, we start by looking at the side notes for E in figure 3.1(g). The parent node for E is C. We continue back-tracing the parent nodes until we hit our starting node. In this example the shortest path is given by

$$A \xrightarrow{5} B \xrightarrow{6} D \xrightarrow{3} C \xrightarrow{4} E : 18. \quad (3.1)$$

3.2 Mode tracing algorithm

The mode tracing tool is composed of several smaller algorithms combined. Figure 3.2 shows the four different steps of mode tracing, which are presented in this section. The first step is to use the PSD calculated for individual time intervals to generate the nodes. Our grid now contains multiple nodes in frequency space for each time interval – each associated with a certain amplitude – as shown in the second step. Next we use Dijkstra’s algorithm to determine the path with the lowest cost (indicated by the blue connection in figure 3.2(c)) to connect all segments with each other and finally plot these points onto a spectrogram.

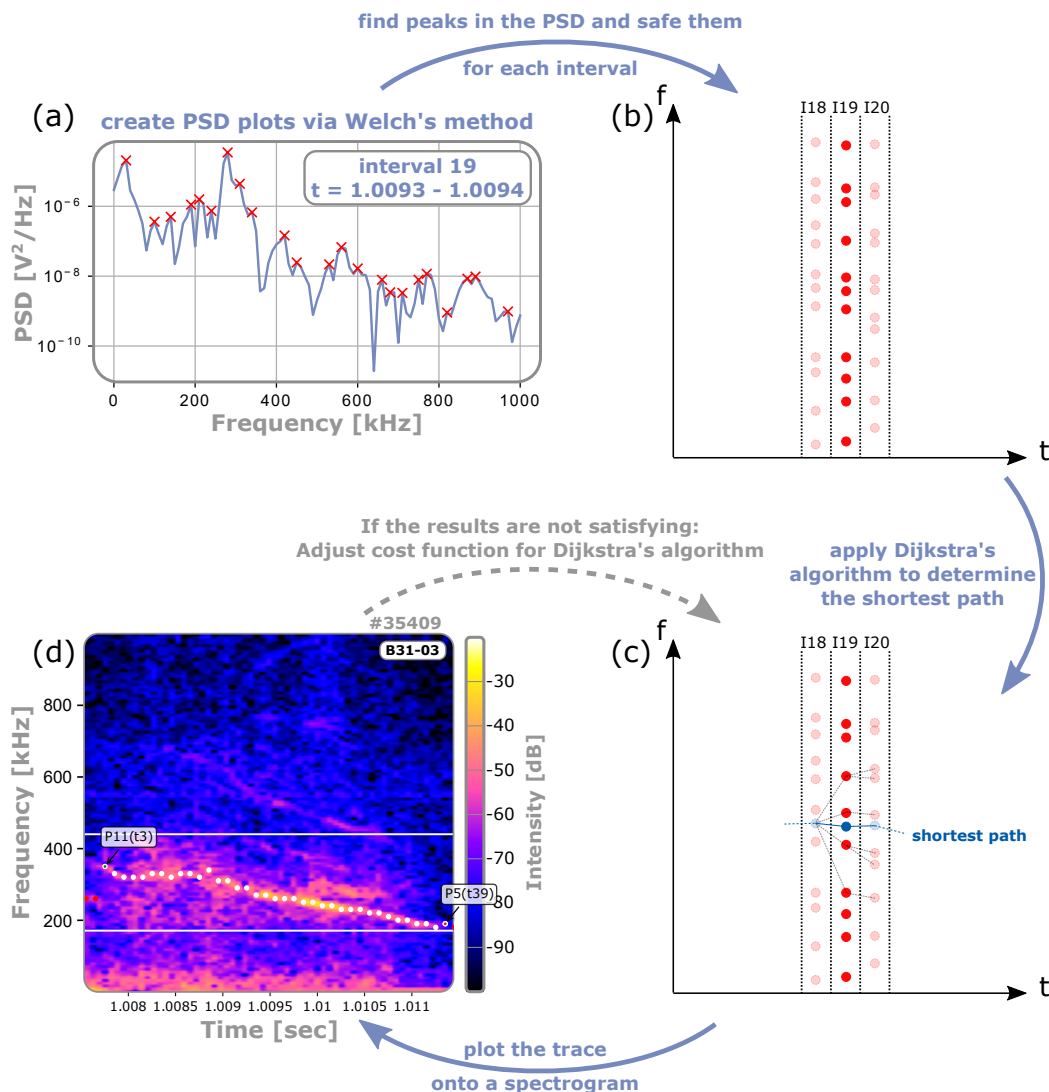


FIGURE 3.2: Sketch of the mode tracking algorithm. The peaks in the PSD serve as the grid-points for Dijkstra’s algorithm. With a cost function the cheapest path is calculated and plotted onto a spectrogram. Via the GUI the user chooses start and end points of the mode.

3.2.1 Initializing the grid via Fourier transformations

To determine the nodes for Dijkstra’s algorithm, the time axis is split into individual sub-windows. For each the PSD is computed via Welch’s method [49] shown in figure 3.2 and 3.3 using the built-in `scipy` module `signal.welch` [58]. For mode tracing purposes only the peak values are of interest for our grid, which are identified by the `scipy` method `signal.find_peaks` (red crosses in figure 3.3). This reduces the number of nodes and ultimately the computing time of Dijkstra’s algorithm. For each time interval an array is created, which includes all of these nodes. The default number of intervals is set to 40. This corresponds to 40 nodes in the final shortest path, plotted onto the spectrogram (white points in figure 3.2(d)). This can be changed by the user; however, the maximum number of intervals is limited by the observed time window. Consequently, the sampling rate of the PSD intervals do not match the sampling rate of the spectrogram.

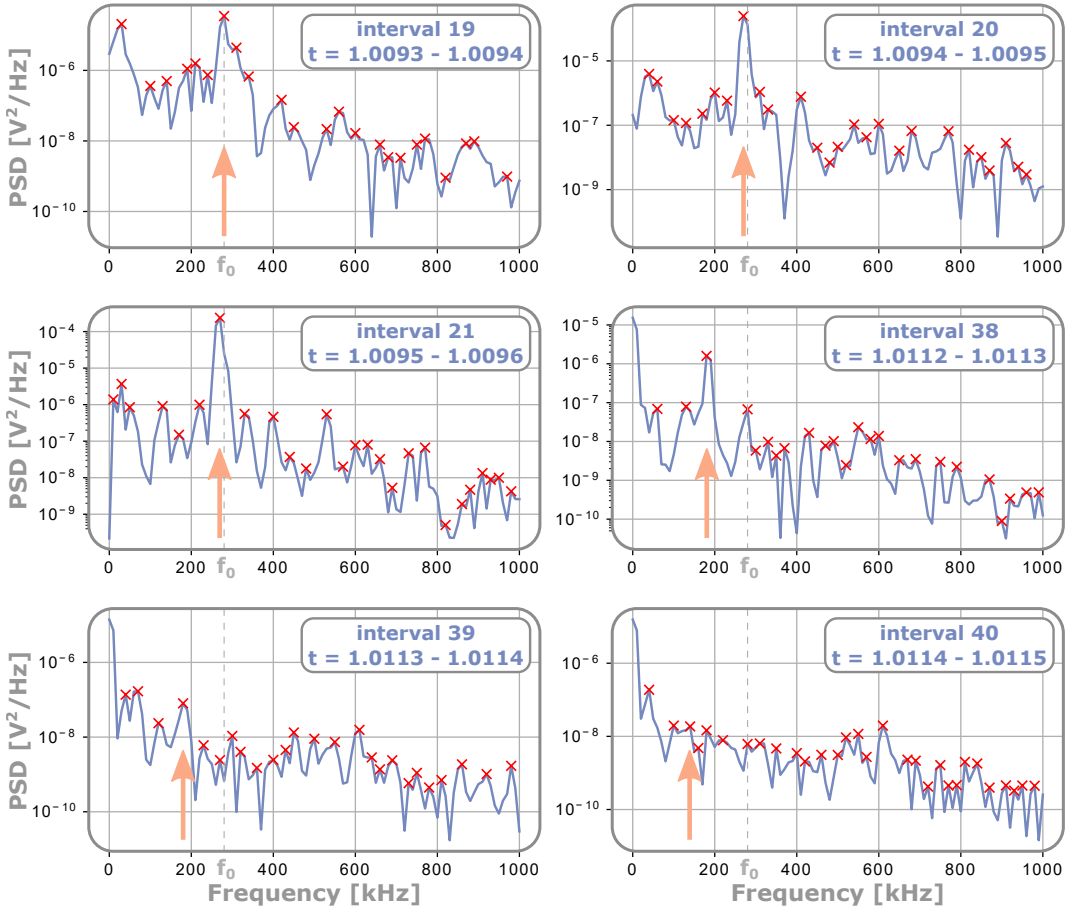


FIGURE 3.3: The time window for discharge #35409 is split into 40 intervals, ultimately corresponding to 40 time-frequency points plotted onto the spectrogram. Excerpt of six PSD plots for different intervals are shown. Indicated by the arrows, the decreasing mode frequency (compared to start frequency f_0) is already visible within the plots.

3.2.2 Framing the data

An upper and lower frequency limit can be manually set in a separate routine, which is referred to as **framing** in the present thesis. The user input from the framing tool shown in figure 3.4 is then passed over to the mode tracing algorithm. This method had to be applied for the analysis of the post disruption modes, as high amplitudes are present in the frequency range below 200 kHz in most cases. Without the restriction to certain time and frequency windows, the mode tracer would often yield undesired results instead of tracing the desired mode. For comparable results and to ensure the PSD-interval creation to work properly, a minimum time window of 4 ms was set by default. However, larger time windows can be set by the user via the lower plot in the GUI, shown in figure 3.4.

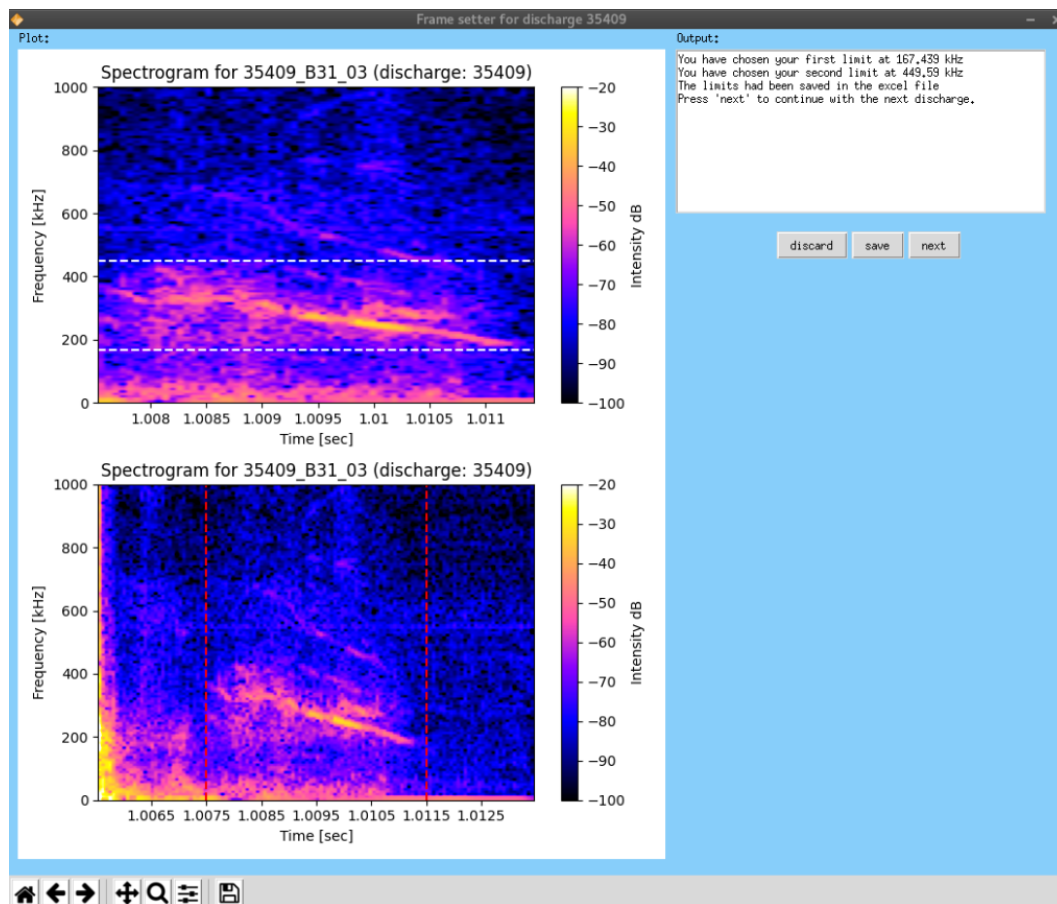


FIGURE 3.4: The GUI of the frame setter. This allows to set the upper and lower frequency limits. Also if the time window is not accurately set (red vertical lines) corrections can be made.

3.2.3 Implementation of Dijkstra’s algorithm

The implementation of Dijkstra’s algorithm used in this work is based on a tutorial [59]. I modified the algorithm to work as an auto-seeded version, thus it does not need a distinct start and end point, but only the start and end time intervals. It traces back the path with the lowest cost for connections from the first interval to the final one. Connections are only initialized for points in the range of the lower and upper frequency limits provided via framing, explained in section 3.2.2. As default values 300 and 800 kHz are set. To assure the continuity of the traced path, only connections with a maximum sweeping rate (df/dt) are initialized. By default this value is given as 1 kHz/ms, but can also be adjusted by user input. Based on the work of Magyarkuti [60], I used a cost function of the form

$$\text{cost}(n \rightarrow n + 1) = c_f \cdot \Delta f + \frac{c_A}{A_{n+1}}. \quad (3.2)$$

It is used to determine the cost for each vertex connecting two nodes in interval n and $n + 1$, respectively. Δf is the absolute change in frequency between the node in interval n and $n + 1$. With this the algorithm is encouraged to prevent large jumps in frequency between intervals, which also preserves the continuity of the trace. A_{n+1} is the amplitude measured for the second node in the node-vertex-node connection. For this part of the function, the cost is minimal for the node with the highest possible amplitude measured for a certain interval. With this the mode tracing algorithm is most likely to trace the high amplitude parts of the mode’s trajectory. c_f and c_A are constants, which can be set by the user as shown in figure 3.5. As a default $c_f = c_A = 10$ is given, which has been found to give good results for the continuity of the traced path, while following the global amplitude maximum of the modes.

Once the path with the lowest cost was determined, the points are plotted onto a spectrogram. The spectrograms are created with the built-in `ax.specgram` method from the `matplotlib.pyplot` module [61]. This method uses the Hann-window as the default window to create spectrograms.

3.2.4 The graphical user interface

Figure 3.5 shows the graphical user interface (GUI) of the mode tracing algorithm. On the top left the spectrogram as well as the points for the shortest path are plotted. The plot underneath it shows the amplitude evolution for the traced path. The user is now supposed to select the desired start (green) and end point (red) by clicking on them. The nodes removed from the shortest path by this selection, now appear in red in the spectrogram and amplitude plot. The labels at the start and end points return the number of the node and the time interval it is located in. For the example in figure 3.5, the selected start is the 17th node (P17 – counting in ascending frequency order) of the second time interval (t2), which is represented by the second point of the shortest path plotted on the spectrogram. Next the user can rate the results of the

mode tracing and add a comment. If the results are not satisfying enough, one can change the weighting coefficients for the cost function from equation (3.2) and recalculate the shortest path. At the bottom right additional information about the modes can be provided by the user, which I used to classify these modes as explained in section 4.1 in more detail. The classification as well as mode parameters are saved into our database.

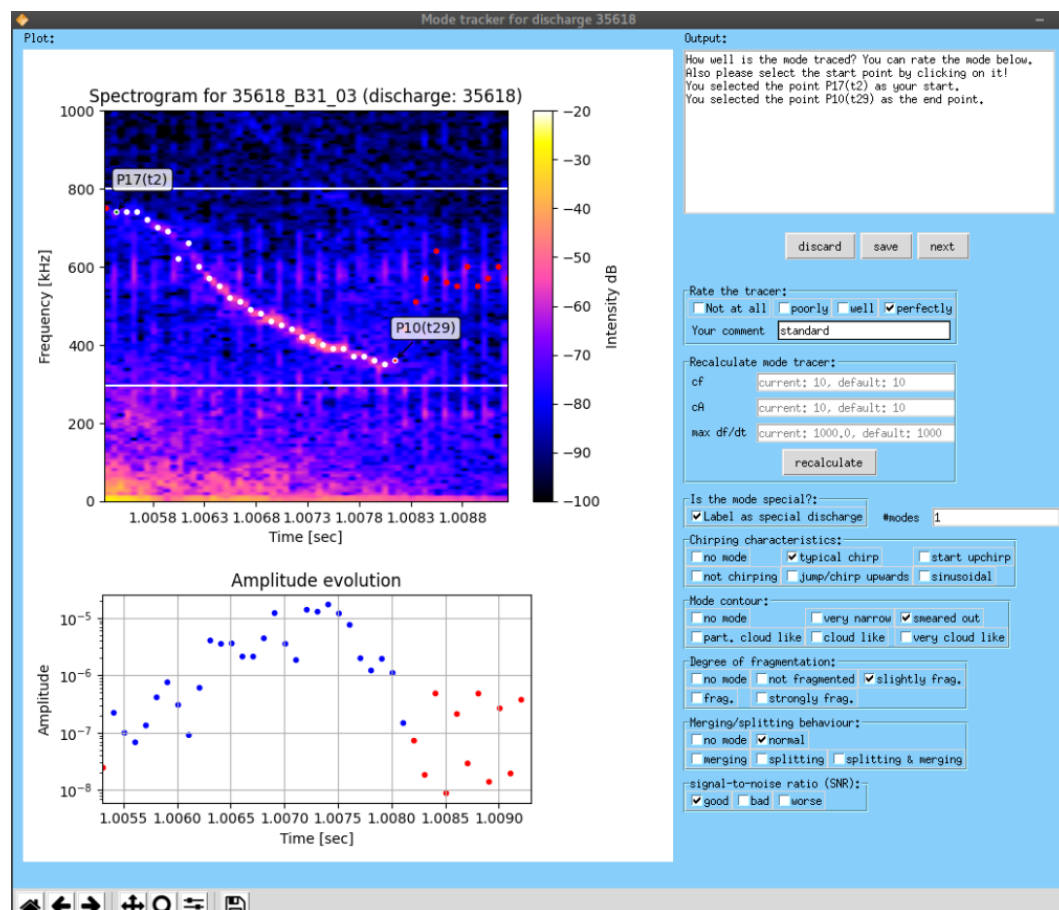


FIGURE 3.5: The GUI of the mode tracker. Start and end points are marked in green and red, respectively. Additional information can be provided with the rating system on the right. If the mode is not sufficiently tracked, the user can recalculate the mode tracing with different weighting coefficients.

3.3 Soft X-ray Amplitude Localization Tool – SALT

To analyze and visualize the different LOSs from the SXR diagnostic, I created a separate tool. The *Soft X-ray Amplitude Localization Tool* (SALT) uses the mode traces, from the algorithm introduced in section 3.2, to access the amplitudes for the desired camera sets of the SXR measurements.

At first, the PSD is calculated as explained in section 3.2 for each LOS. Now the amplitudes – at the desired frequencies given by the mode’s trace – are extracted. In addition the root mean squared (RMS) for the raw signals is calculated, which is used to generate the profile and fit a quadratic function to it. From this fit the gradient at each position of the LOSs is used to normalize the signals. This is necessary as the local fluctuations are most likely not caused by density or temperature fluctuations directly, but rather fluctuations of the magnetic surfaces themselves. Consequently, the change in SXR emissivity is proportional to the displacement and gradient given by the underlying SXR profiles [50]. The poloidal cross section of the vessel with the LOSs is plotted and the individual LOSs are color-coded by magnitude of the SXR amplitude at the mode’s frequency. This is done for each time interval, thus the user is also able to access the time evolution of this amplitude visualization.

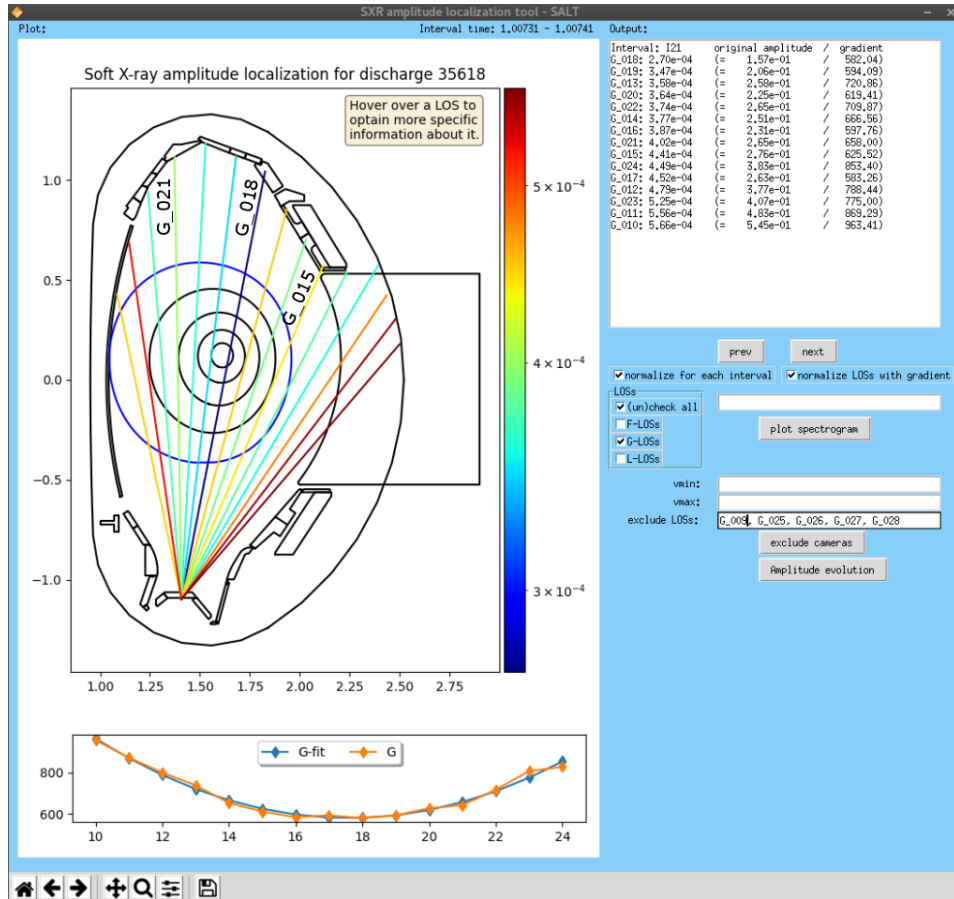


FIGURE 3.6: The *Soft X-ray Amplitude Localization Tool* – SALT, is used to visualize the amplitude of the SXR at the mode’s frequency. The plot at the top shows the individual LOSs with amplitude color-coding. The signals RMS is displayed at the bottom and a quadratic fit is applied to obtain the gradient for each LOS. This gradient can be used to normalize the signals as indicated by the option *normalize LOSs with gradient*. With the respective buttons *prev* and *next* the user is able to access the time evolution of the profiles and amplitudes.

Chapter 4

Observations and results

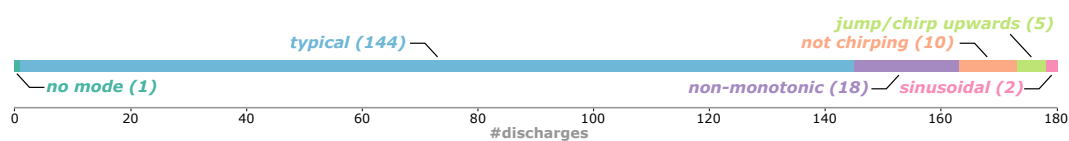
In this chapter the observations and results are presented. At first, five mode characteristics are introduced in section 4.1 used to classify the underlying data set. In section 4.2 the time window in which those modes appear is given, followed by the mode’s behaviour in incomplete disruptions in section 4.3. Section 4.4 covers the spatial localization of these modes and lastly the results from the coherence & mode number investigations are shown in section 4.5.

4.1 Mode characteristics

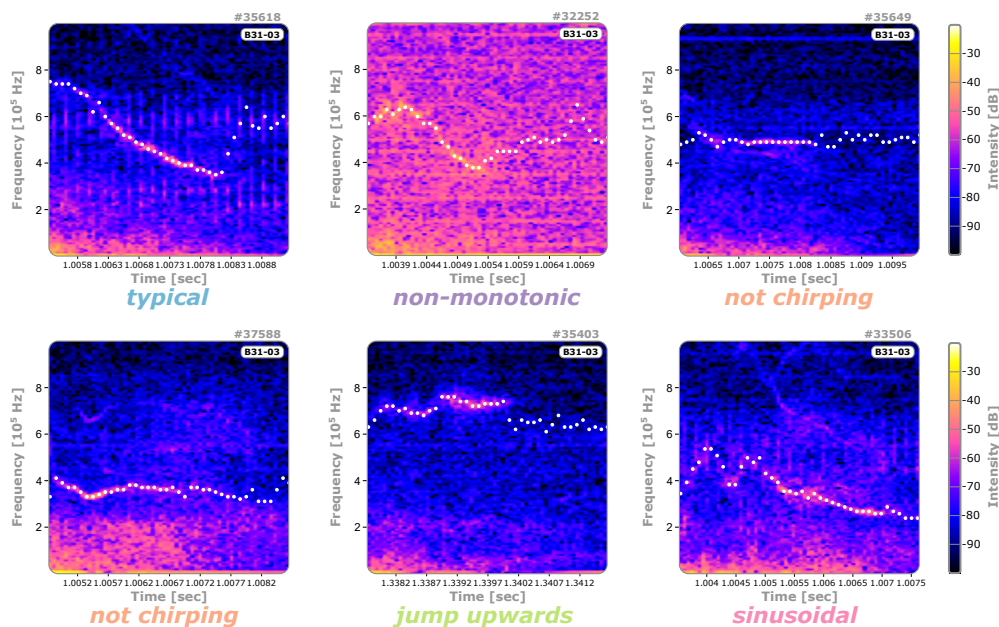
I used the mode tracing tools presented in chapter 3 to extract mode characteristics, and also to categorize mode behaviour. The mode properties form the basis of the database analysis in chapter 5. To classify those modes, I highlighted five different mode characteristics, which are introduced and explained in more detail in the following sections. They were developed as I went through all 180 discharges with my tools. I categorized them by hand, thus the individual rating of each mode is subject to my personal view.

4.1.1 Sweeping behaviour

The first and most prominent characteristic of these modes is their sweeping behaviour. As the mode evolves in time, its amplitude and frequency changes. This typically results in a frequency evolution, where the mode starts at higher frequencies – often around 800 kHz – and chirps towards lower frequencies. The change in frequency is typically strongest at the beginning and reduces towards the end of the mode. This evolution is the most common type of sweeping behaviour as shown in figure 4.1(a), thus is referred to as **typical** throughout this thesis. This behaviour is also observed for both DIII-D cases shown in figure 1.5(c, d). The discharge #35618, representing this kind of sweeping behaviour, is used as my reference example and has been analyzed in more detail, also with the help of simulations. If the time evolution is initiated by an increase in frequency first, followed by the typical evolution, this is referred to as a **non-monotonic** mode. For ten cases inside our database we observe



(a) Distribution of different sweeping behaviours.



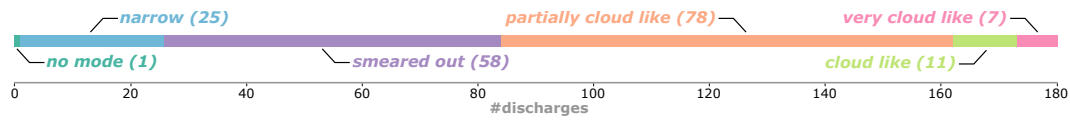
(b) Examples for each sweeping behaviour.

FIGURE 4.1: The sweeping behaviour of the modes. In (a) the distribution of sweeping types is depicted. In (b) examples for each type are given.

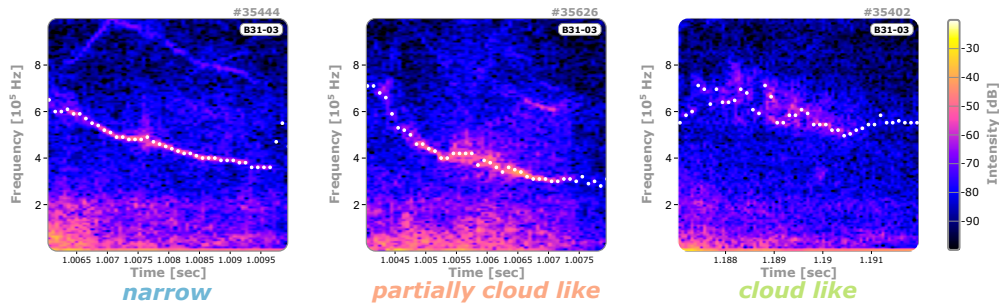
modes, which fluctuate around a certain frequency or do not chirp at all. Five modes show an increase in frequency as the mode continuously chirps upwards or depicts a jump in frequency. In two discharges we observe a mode, which starts with an up- and down-chirping behaviour, similar to the evolution of a sine function and followed by the typical sweeping behaviour. Consequently, those two examples are labeled as **sinusoidal** as shown in figure 4.1.

4.1.2 Mode contour

Another important characteristic of these modes is the sharpness of the mode contour. Cases exist – referred to as **narrow** – which depict a sharp contour, thus have a well defined frequency. The more the modes lose their sharp contour as the spectral width broadens, the harder it is to determine their main frequency. **Smearred out** modes depict a frequency evolution which is still well traceable. If the main frequency is hard to determine, as the mode does not show a distinct contour any more, the mode is referred to as (**very**) **cloud like**. If at least a short fragment of the mode shows this cloud like behaviour but the rest is well traceable, it is labeled as **partially cloud like**.



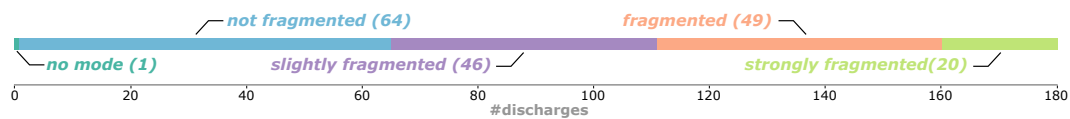
(a) Distribution of different mode contours.



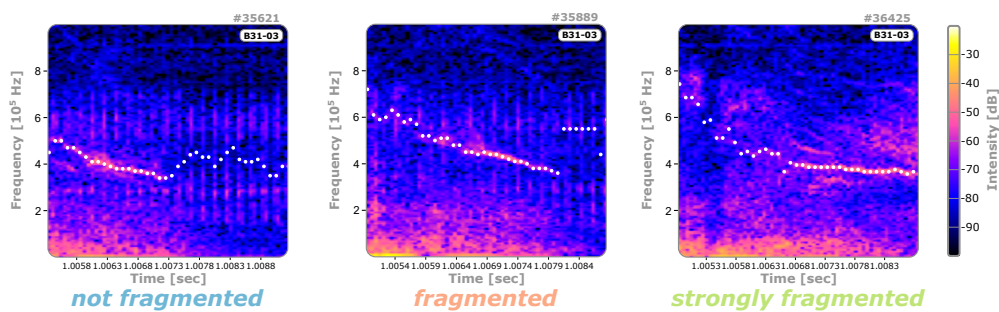
(b) Examples for the different mode contour definitions.

FIGURE 4.2: The mode contour characteristic. In (a) the distribution of the mode contour is depicted. In (b) examples for mode contour types are given.

4.1.3 Degree of fragmentation



(a) Distribution of different degrees of fragmentation.



(b) Examples for the different degrees of fragmentation.

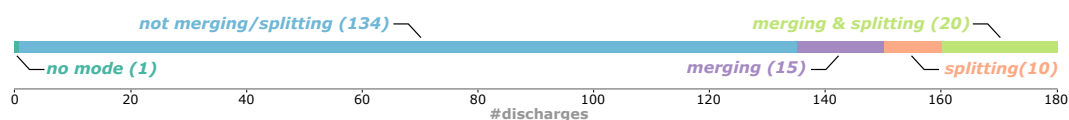
FIGURE 4.3: The degree of fragmentation. In (a) the distribution of each degree of fragmentation is depicted. In (b) the degree of fragmentation is shown by examples.

Modes can also show fragmentation effects which are classified by the **degree of fragmentation**. It indicates, how continuously a mode evolves in time and how many intersections appear. The higher the degree of fragmentation, the harder it is to trace the mode's amplitude and frequency evolution. This parameter also depends on the position of the magnetic coil. The distribution given in figure 4.3(a), shows the degree of fragmentation for the reference coil

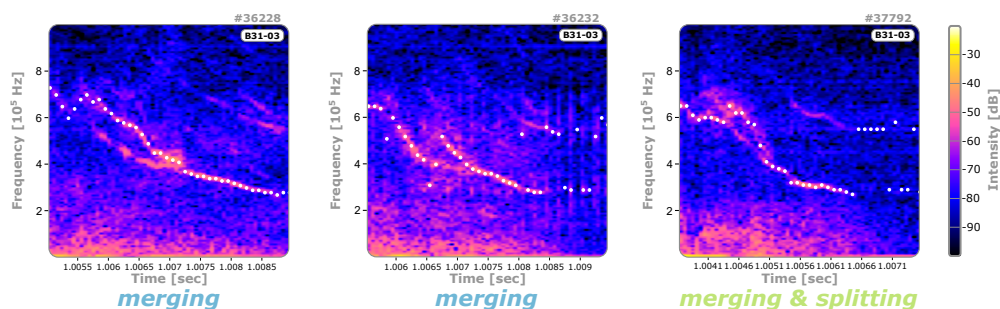
B31-03 (see section 2.1) in most cases. Only if the mode tracing precision is significantly increased, the modes are traced in other coils or in the SXR for a few discharges.

4.1.4 Merging & splitting of modes

In some discharges modes are present, which split into two mode branches or emerge from them. If two modes appear within a discharge, they mostly merge at a certain point in time. For most discharges we observe no merging or splitting behaviour as shown in figure 4.4(a).



(a) Distribution of merging and splitting of modes.

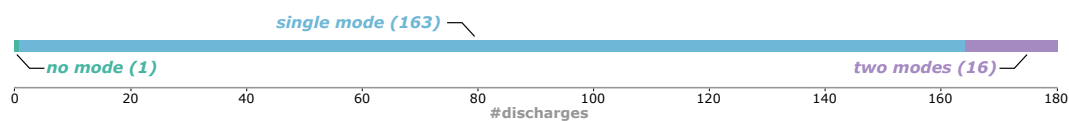


(b) Examples for merging and splitting of modes.

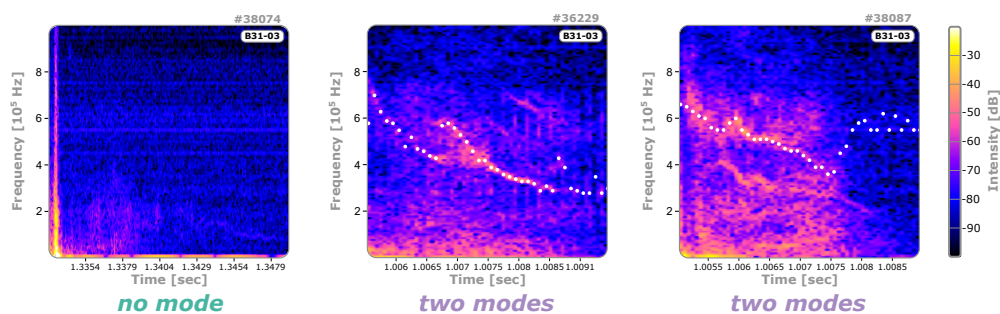
FIGURE 4.4: Mode merging and splitting. In (a) the distribution of the merging and splitting properties is depicted. In (b) examples for mode merging as well as splitting are provided.

4.1.5 Number of modes

The last characteristic, which has been analyzed for all 180 discharges is the number of modes appearing during the experiment. For most discharges we observe single modes and often their upper harmonics as shown in figure 4.5(a). For this classification the number of harmonics is not taken into consideration, thus only the number of distinct modes was investigated. For 16 discharges in our database we observe two modes. Nearly all of them merge at a certain point in time, around 30 – 55% of the total mode time as depicted by #36229 in figure 4.5(b). Only for discharge #38087 (figure 4.5(b)) we observe two modes, which do not necessarily seem to be upper harmonics but are vertically separated. The only discharge, which seems not to contain any modes is #38074. Neither in the magnetics nor in the Soft X-ray LOSs any activity is visible. However, the global parameters do not show any significant differences to the other discharges from the same session.



(a) Distribution of number of modes which appear inside each discharge.



(b) Examples for number of modes.

FIGURE 4.5: The number of modes in the experiments. In (a) the distribution for the number of modes is depicted. In (b) the spectrograms for discharge #38074 (no mode) as well as discharges with two modes are provided. #38087 is the only discharge which shows the presence of two strong modes which do not merge at any time.

4.2 Mode time frame

We can use the modes' traces to plot the mode frequency evolution against the time displayed in figure 4.6. In this plot all 179 time traces are plotted against the time, represented in percent of the current quench time window as defined in section 1.2.1. The color-coding shows the different sweeping behaviours defined in section 4.1.1 and in addition the discharge #35618 is highlighted as a reference. As illustrated in figure 4.6, the mode's time traces are **exclusively** located inside the current quench phase. Consequently, this mode will be also referred to as **current quench mode** (CQ-mode) within this thesis. In addition – despite the different mode characteristics – they depict high self-similarity. For about 87% of all discharges, a time window of the default 4 ms is chosen to trace the mode. Therefore, only for a small fraction, the time window was chosen larger than the 4 ms. The time window was subdivided into 40 intervals for all of these discharges, thus most discharges share the same sampling frequency of the mode traces. In addition the frequency sampling of the function `signal.welch` as introduced in section 3.2.1 depends on the duration of the individual intervals. This results in the same time and frequency sampling only for the majority of discharges within the database. This is also visible in figure 4.6 as certain bars of the frequency histogram are enlarged. Therefore, the periodically appearing strong deviations from a smooth distribution could be linked to this sampling and the bin size of 10 kHz for the histogram. In figure 4.6(b) the mode traces are not displayed as a line plot, but instead each individual time-frequency point is plotted to illustrate

this sampling effect. As indicated by the red circle, not all frequency points share the same frequency sampling.

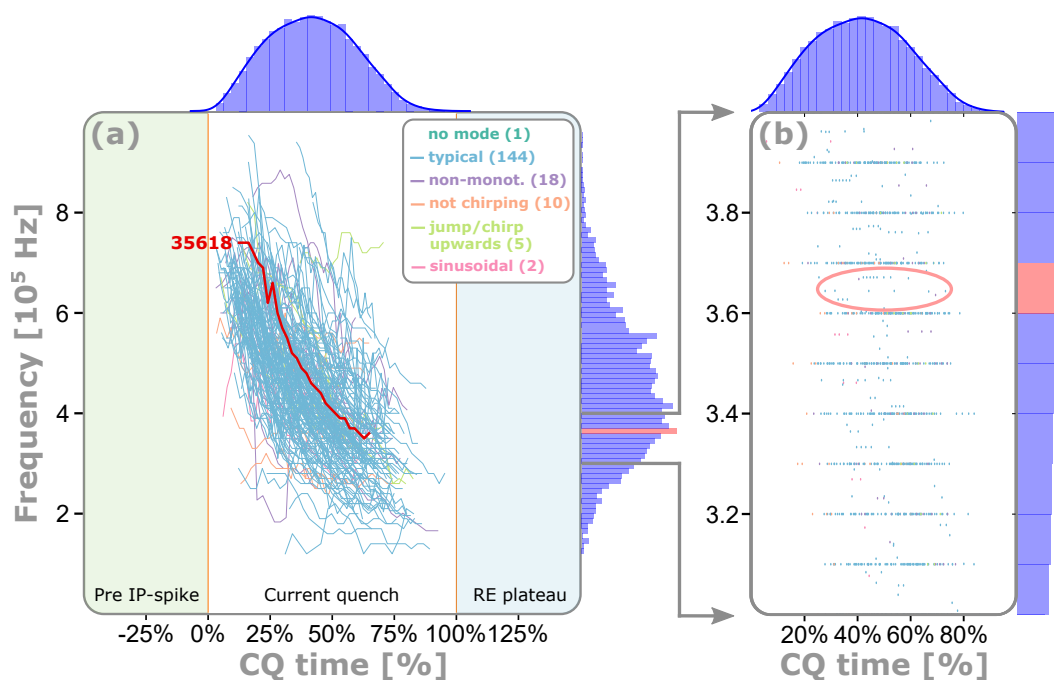


FIGURE 4.6: Time window of the mode appearances. In (a) the mode frequency traces are plotted against the CQ-time in percent. The modes are located exclusively inside the current quench. The time evolution for the reference discharge #35618 is highlighted. In (b) the effect of the frequency sampling is shown. More details are given in the text.

4.3 Mode behaviour in incomplete disruptions

Our database includes five discharges, which show incomplete disruptions as multiple IP-spikes appear. Figure 4.7 shows the time evolution of an example discharge, presented the same way as in section 1.2.1. The initial IP-spike also marks the start of the CQ. In addition we observe a second one about 3 ms after the first. As shown in the spectrogram of the coil B31-03, the mode is only present after the **last** IP-spike had occurred. Also for the other four incomplete disruptions inside our database the mode does not show any activity in between the IP-spikes. Consequently, it seems to be at least not dependent on gradients or thresholds in the plasma current evolution alone, but is rather triggered by a more complex interplay of events.

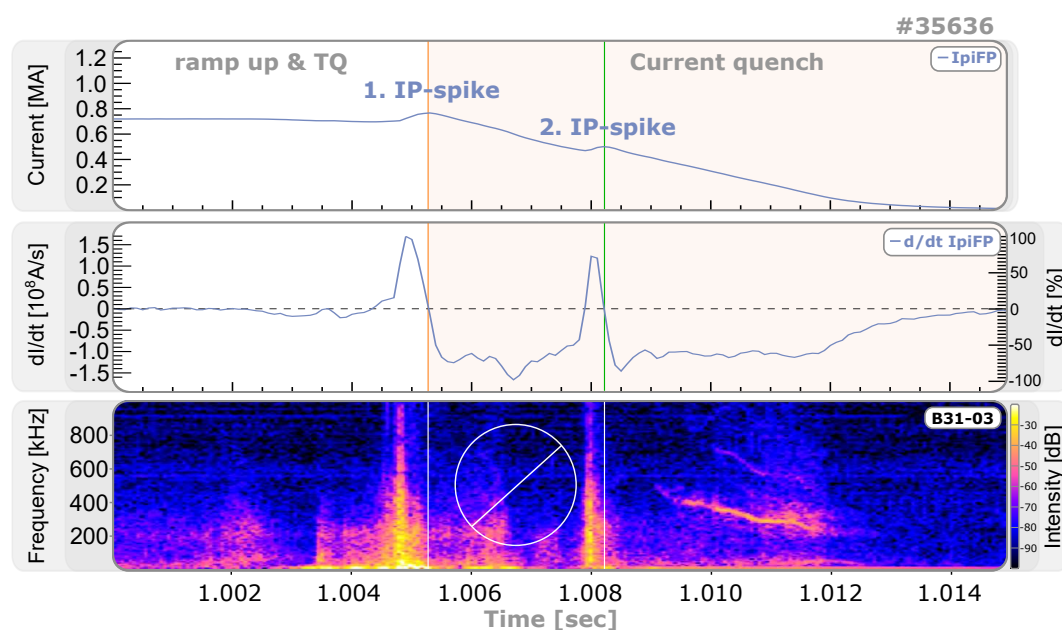


FIGURE 4.7: Behaviour of the modes in incomplete disruptions. The mode always appears after the **last** IP-spike had occurred.

4.4 Localization of the modes

In this section, the results from mode localization investigations are presented. This was done using the magnetic coils (see section 2.1) and SXR measurements (see section 2.2). In figure 4.8 the mode amplitudes and the background activity for the magnetic coils are given. This plot for the magnetic coil sets C09 and B31, was created by hand, as I was still developing the mode tracing tools in parallel. I plotted a spectrogram for each coil and estimated mode and noise amplitudes. While the upper-right triangle shows my estimate for the CQ-mode amplitudes, the lower triangle represents amplitudes of different activity, often appearing below the mode frequency. Based on the visibility of the CQ-mode, the magnetic coil B31-03 was chosen as the reference coil in the early stages of the investigations. It is located at the LFS midplane. The coil B31-14 is located closer towards the plasma surface, showing enhanced mode amplitudes, but also higher background noise, thus the SNR is similar. Therefore, this coil was chosen as a substitute coil for a few discharges within the database. The tool **SALT** from section 3.3 was used to determine the amplitudes for each camera set of the SXR measurements in the later phase of my research. The modes are visible in every camera set, even for high runaway currents, thus saturation by hard X-ray radiation seems to be no issue. Camera set G yields the most interesting results. The amplitudes are typically strongest around the edge channels G_015 and G_021 compared to the central LOS G_018, shown in figure 4.9 and also highlighted in figure 4.11. However, for the LOSs from camera F – which shares the same poloidal angles, but located at a different toroidal position – this trend is not visible. For camera F,

the core channels also display a strong mode activity as shown in figure 4.10. The cause of this phenomenon is still under investigation.

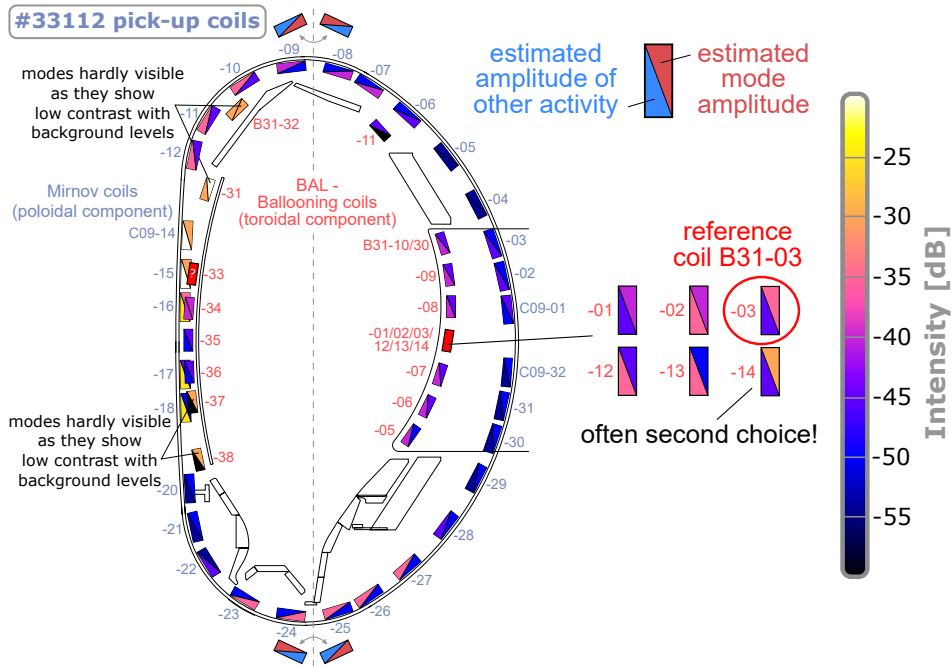
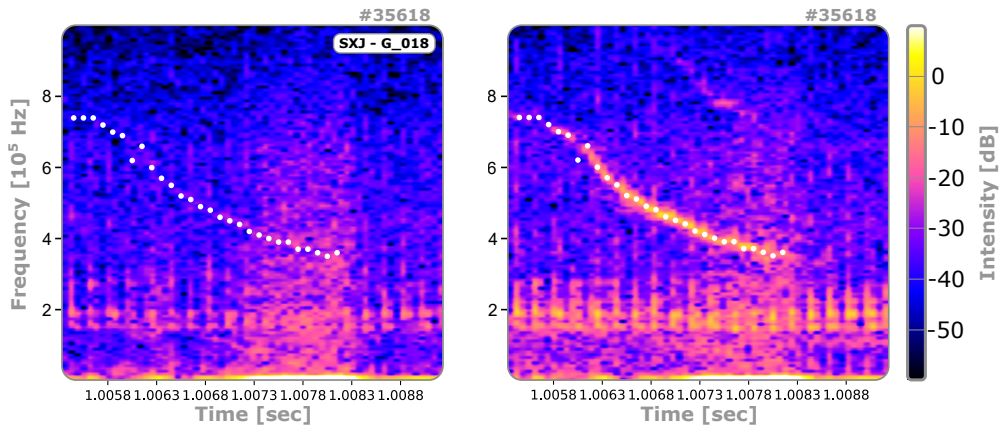


FIGURE 4.8: The estimated amplitudes of the CQ-mode and other activity inside spectrograms for magnetic pick-up coils. The color-coding of the upper-right triangle represents the estimated CQ-mode amplitude, while the lower one shows the activity typically below the mode frequency. The amplitudes are given for Mirnov- (blue, outer coil set) and BAL-coils (red, inner coil set) for my initial reference shot (#33112).



(a) Spectrogram for LOS G_018

(b) Spectrogram for LOS G_015

FIGURE 4.9: Spectrograms for different LOSs of the SXR measurements. G_018 (a) is directed into the core region, while G_015 (b) is closer to the plasma edge.

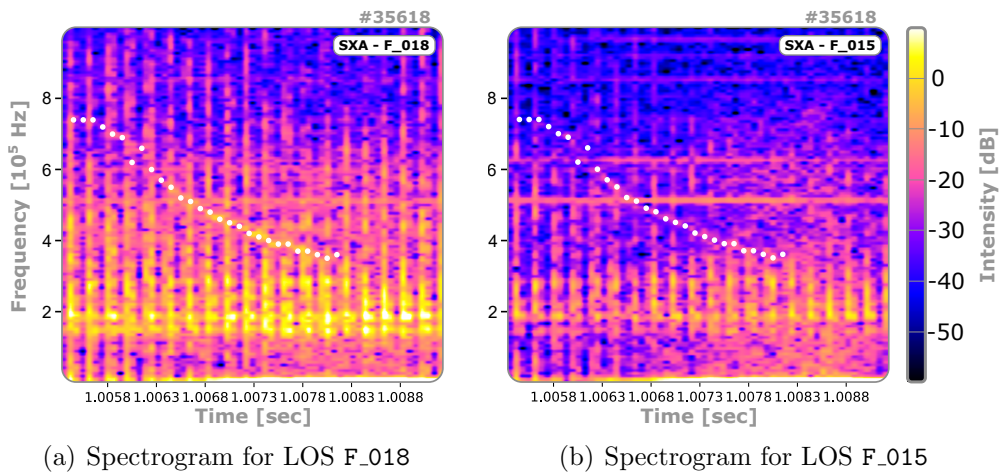


FIGURE 4.10: Spectrograms for different LOSs of the SXR measurements. F_018 (a) is directed into the core region, while F_015 (b) is closer to the plasma edge.

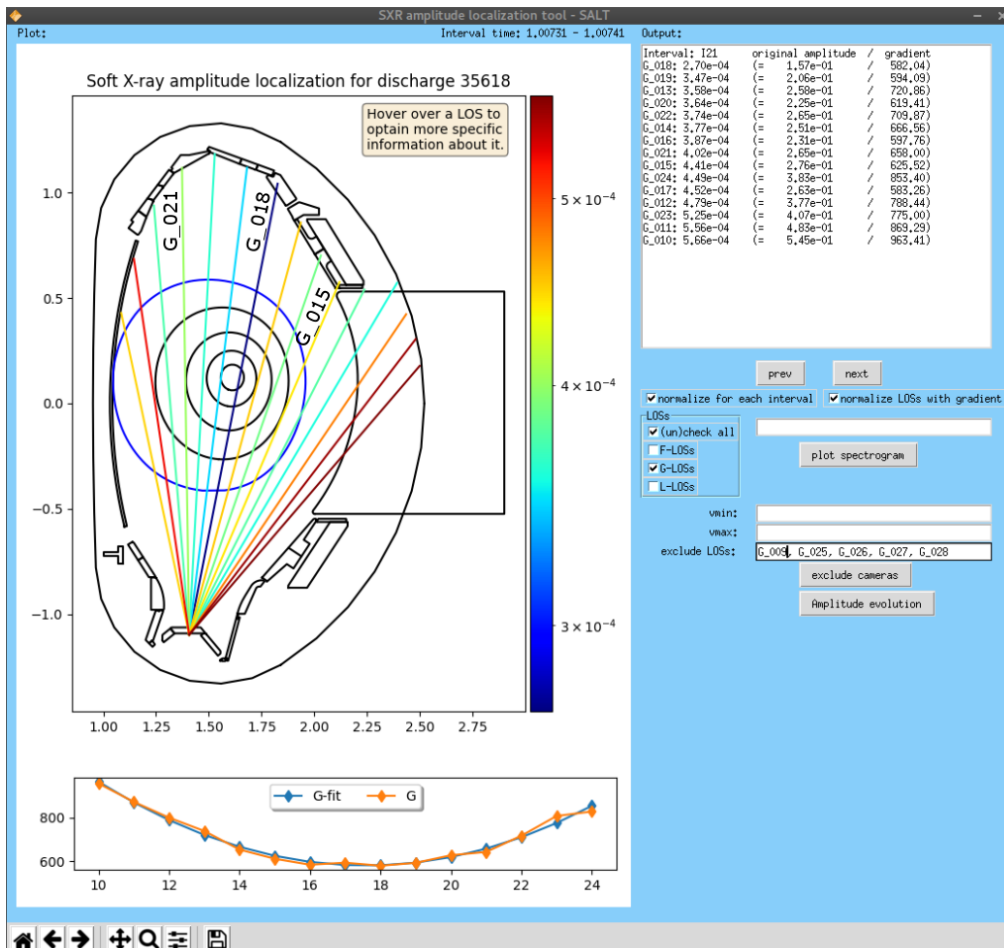


FIGURE 4.11: Visualization of the amplitudes inside the SXR measurements by SALT. The amplitudes around the edge channels G_015 and G_021 are typically strongest.

4.5 Coherence & mode numbers

To close this chapter about the experimental results, the coherence and mode number investigations are briefly discussed.

As a large set of magnetic coils inside the vacuum vessel is available for ASDEX Upgrade, coils at different toroidal and poloidal positions can be used to determine the coherence and mode numbers of these modes [52]. In figure 4.12(a) the minimum coherence plot for toroidally distributed coils is shown, with the mode being highlighted. In a minimum coherence plot, the coherence is calculated for all possible pairings of signals measured by the magnetic pick-up coils. As the final step, the smallest of these values for each time step is plotted. Illustrated by our reference discharge in figure 4.12(a), the coherence in the coils is large at the modes' frequencies. Consequently, the modes can be considered as globally coherent. In figure 4.12(b) the toroidal mode number analysis for our reference discharge is displayed. The displacement $\xi(\vec{r})$ from the equilibrium can be written as

$$\xi(\vec{r}, t) = \vec{\xi}(r) \cdot \exp[i(m\theta + n\phi - \omega t)] \quad (4.1)$$

with the displacement vector $\vec{\xi}(r)$ [19]. Hereby, the integers m and n represent the poloidal and toroidal mode numbers of the perturbation, respectively. For our definition, the sign of n is linked to the propagation direction of the mode. The mode numbers could not be pinned down to single values of n – which is also valid for all other examined discharges – as the mode seems to be composed by a mixture of many different mode numbers. However, the most prominent ones seem to be $n = 0$ and $n = -4$. Hereby, for a negative n value, the propagation of the mode is in the ion diamagnetic direction.

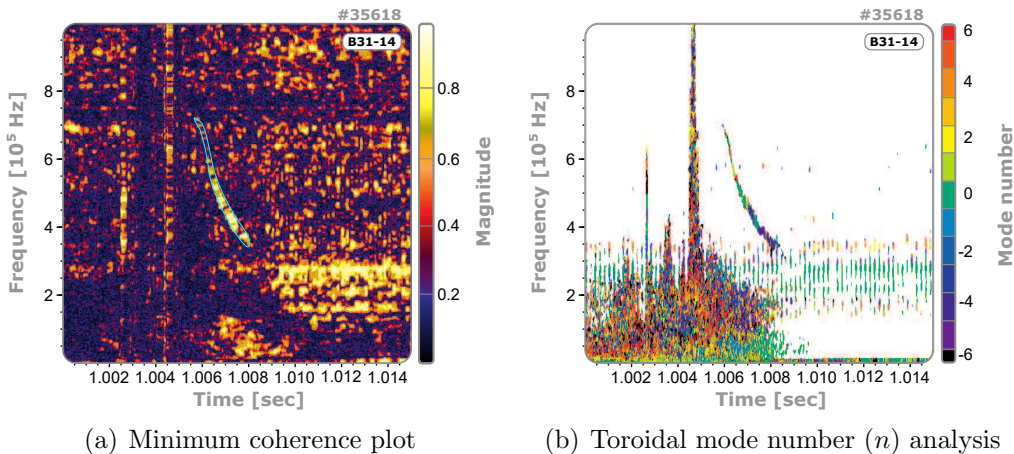


FIGURE 4.12: The minimum coherence plot (a) and mode number analysis (b) for discharge #35618. While the modes are globally coherent, the toroidal mode number is a mixture of multiple n with $n = 0$ and $n = -4$ being the most prominent ones. The plots were created by Gergely Papp using the NTI Wavelet Tools package [52].

Chapter 5

Statistical analysis of the mode characteristics

Statistical analysis is a powerful concept for observing trends and investigating possible correlations within databases. In this chapter I introduce our database consisting of 180 discharges with the primary goal of runaway electron generation and summarize my data analysis results. In section 5.1, this database created by the tools from chapter 3, is presented. In section 5.2 the concept of "most likely frequencies" is explained. In section 5.3 data analysis methods are introduced and results discussed. Finally, the main take-away points of chapter 4 and 5 are collected in section 5.4.

5.1 The database

The database mentioned in section 2.3 is presented in more detail now. With the help of the mode tracing tool, I analyzed all 180 discharges. The acquired data was saved into an excel file, which also contains a large set of global parameters. This includes for example the plasma and subsequent RE-current, toroidal magnetic field strength, plasma temperature, q_{95} value or density measurements. An excerpt of the parameters is shown in table 5.1 and within the correlation matrix in figure 5.3. The mode tracing tool (MTT) does not only provide the frequency and amplitude evolutions for these modes, but also determines the start and end times. In addition the classification for all 179 modes by their mode characteristics presented in section 4.1 is also included inside this database. This data was used together with the global parameters to search for trends by statistical analysis which is explained in more detail in section 5.3.1 and 5.3.2.

PARAMETER DESCRIPTIONS

parameter [unit]	description
shotnr	ID of the discharge. The routine/setup might change between discharges.
t_{trigger} [s]	Time when the MGI valve was triggered. $t_{\text{trigger}} = 1.0$ s for 160/180 discharges.
dt_{mode} [ms]	Duration of the mode given by the MTT.
$t_{\text{IP}} - t_{\text{trigger}}$ [ms]	Time point of the initial IP-spike.
$t_{\text{mode start after 1. IP}}$ [ms], $t_{\text{mode end after 1. IP}}$ [ms]	Start & end time of the mode with respect to the initial IP-spike
$t_{\text{last IP}} - t_{\text{trigger}}$ [ms]	Time point of the last IP-spike for incomplete disruptions.
$t_{\text{mode start after last IP}}$ [ms], $t_{\text{mode end after last IP}}$ [ms]	Start & end time of the mode with respect to the last IP-spike
$t_{\text{end CQ}} - t_{\text{trigger}}$ [ms]	End time with respect to the trigger time.
dt_{CQ} [ms]	Length of the CQ. Defined by the initial IP-spike and end point (see section 1.2.1).
$f_{\text{mode start}}$ [kHz]	Starting frequency of the mode.
$f_{\text{mode end}}$ [kHz]	Frequency at the end of the mode.
df [kHz]	Change in frequency $f_{\text{mode end}} - f_{\text{mode start}}$
average f [kHz]	Average mode frequency derived by the arithmetic mean.
most likely f [kHz]	Most likely frequency of the mode (see section 5.2).
A_{min} [dB], A_{max} [dB]	Minimum/Maximum mode amplitude.
dA [kHz]	Difference in mode amplitude $A_{\text{max}} - A_{\text{min}}$.
sweeping char. ¹	Rating of the sweeping characteristic from typical (1) – sinusoidal (5) and no mode (0).
contour ¹	Rating of the mode contour from narrow (1) – very cloud like (5) and no mode (0).
deg. of fragm. ¹	Rating of the degree of fragmentation from not fragmented (1) – strongly fragmented (5) and no mode (0).

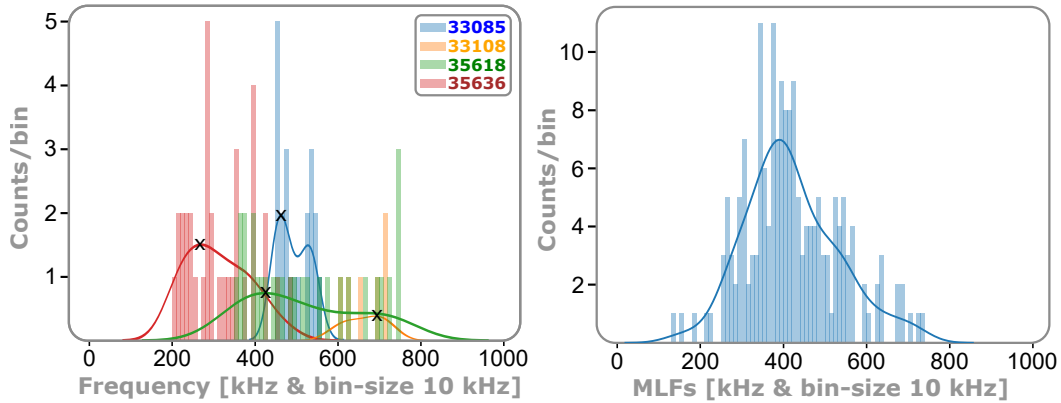
¹The characteristics are introduced in section 4.1

parameter [unit]	description
merging/splitting ¹	Rating of the mode merging & splitting behaviour from not merging nor splitting (1) – splitting and merging (5) and no mode (0).
#modes ¹	Number of prominent modes inside the CQ.
I_{P0} [MA]	Pre-disruption plasma current.
I_{RE} [kA]	Runaway current after the CQ.
dI [kA]	Difference between the pre-disruption and runaway current.
NZ [bar]	Amount of MGI gas injected.
B_{tor} [T]	Toroidal magnetic field strength.
q_{95}	Value of the safety factor (eq. (1.6)) at $\rho_{pol} = 0.95$.
NBI-source 3/7/8 active?	States whether the respective NBI source 3, 7 and 8 is active (0 = not active, 1 = active).
P_E [MW]	Average heating power by ECRH before the valve is triggered.
W_E [kJ]	Plasma stored energy.
T_e [keV]	Electron temperature measured by ECE-measurements.
n_{pre} [10^{19} m^{-3}]	Pre-disruption plasma density measured by CO ₂ interferometry (LOS: V-1).
n_{post} [10^{19} m^{-3}]	Post-disruption plasma density measured by CO ₂ interferometry (LOS: V-1).
n_{max} [10^{19} m^{-3}]	Maximum plasma density measured by CO ₂ interferometry (LOS: V-1).
MGI gas type	One of the following four gas types are used for the MGI: Ar, Ne, Kr or Xe with numbers 1–4 assigned.

Table 5.1: Excerpt of parameters inside the database.

5.2 Most likely frequencies

An important parameter, which might enable a future external mode drive, is the **most likely frequency** (MLF). It represents the mode's frequency, which is maintained for the longest duration. As these modes often chirp strongest at the start, the MLFs are not necessarily given by the arithmetic mean. Therefore, the individual MLF for each discharge was determined via histograms with a bin size of 10 kHz. In figure 5.1(a) histograms for four different discharges are shown. For each of those discharges, the individual probability density function (PDF) was calculated. The MLF is determined by the global maximum of this distribution, indicated by the black crosses in figure 5.1(a). The distribution of the 179 MLFs for each discharge is shown in figure 5.1(b). The maximum is located at 340 and 370 kHz, respectively. Therefore, the most probable resonance frequency for externally driven modes is slightly below 400 kHz.



(a) Histograms to determine the individual MLF for each discharge. (b) Distribution of MLFs for all 179 modes.

FIGURE 5.1: Most likely frequencies of the modes. In (a) the determination of the individual MLF for each discharge via histograms is illustrated. The overall distribution of these frequencies is shown in (b) with a maximum at 340 and 370 kHz, respectively.

Figure 5.2 shows a comparison between the MLF and the average frequency determined by the arithmetic mean. The dashed line represents, where the most likely and average frequency matches. Points above this line depict discharges with higher MLF, while the average frequency is higher for points below it. As shown by this plot the average frequency typically overestimates the MLF, which is due to the sweeping behaviour. Most modes start with a strong frequency chirp, which flattens over time, thus the MLF is located closer to the end-frequency of the mode. Consequently, the start frequency influences the (absolute) change in frequency most, while the end frequency has the most impact on the MLF.

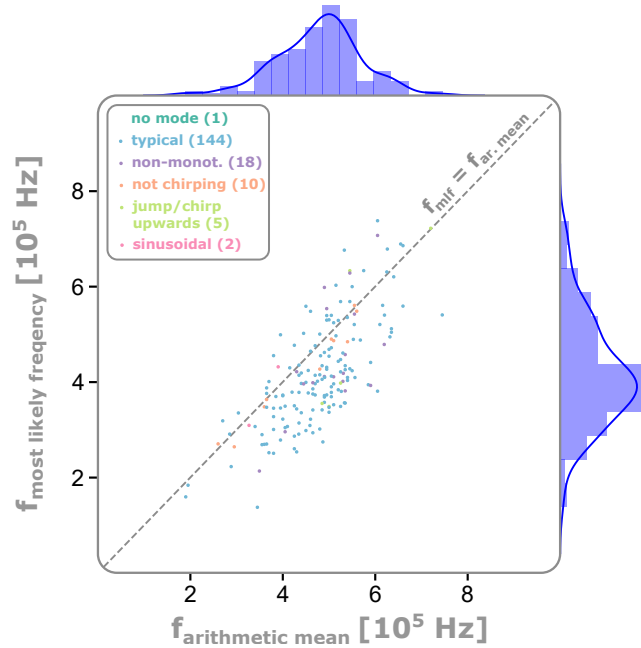


FIGURE 5.2: MLFs plotted against the average frequency determined by the arithmetic mean. The average frequency typically overestimates the MLF, due to the sweeping behaviour.

5.3 Statistical analysis methods

In this section three statistical analysis methods are introduced, which were used to examine our database. First the analysis with a correlation matrix is introduced, followed by the factor analysis and regression concept.

5.3.1 Correlation matrix

A good first step to analyze a database is to use a correlation matrix. It is able to yield overall trends within the global parameters; however, does not account for the individual time evolution of parameters within a discharge. A technique to investigate trends in e.g. the time, frequency or amplitude evolution itself is given by the regression analysis in section 5.3.3. The correlation matrix of our database, shown in figure 5.3, was created with the method `pandas.DataFrame.corr` [62]. Pearson's correlation is used, which yields the strength and direction for the linear relationship between two continuous coefficients [63]. The correlation value (Pearson's r) is expressed by

$$r_{xy} = \frac{\text{cov}(x, y)}{\sqrt{\text{var}(x)} \cdot \sqrt{\text{var}(y)}} \quad (5.1)$$

with the covariance of x and y , as well as their variance [63]. It can take values between -1 and 1. It is important to emphasize, that this does **not** correspond to the slope of the linear fit of this relation! The color-coding in

figure 5.3 expands from 1 (fully correlated) in red, over 0 (no correlation) in white, towards -1 (fully anti-correlated) in blue. The principal diagonal always shows the auto-correlation of the parameter, thus depicts a correlation value of 1 and acts as the symmetry axis of the matrix. The present correlation matrix includes the start and end times of the modes (in different reference frames), such as the timing with respect to the current quench time or the time window initiated by the trigger of the MGI valve. It also contains information about the mode frequency and amplitude as well as the mode characteristics defined in section 4.1. Examples for global parameters are the plasma current, q_{95} or heating power. A detailed description for each parameter is given in table 5.1. The discharges #33084/85 use a different MGI valve, thus the trigger time and the actual gas penetration time differ by a lot. Those discharges lead to correlations values, which deviate strongly from the main trend within the database, thus had been excluded. In figure 5.3 I also highlighted four regions of interest, which will be analyzed in more detail now.

Region 1 shows high (positive) correlation values, thus is one of the first regions drawing the attention onto it. It is attached to the principal diagonal, therefore it shows the correlation results for factors close to each other in the factor list. It depicts the three blocks of time-, frequency- and density-components. Let us pick the frequency block as an example. If we have a high starting frequency ($f_{\text{mode @start}}$ [kHz]), the difference in frequency (df [kHz]) and also the average frequency (average f [kHz]) is more likely to be high. As a result, their correlation value is close to +1. Similar internal connections also apply to the other blocks of region 1.

For **region 2** this is not the case anymore. It is located far from the principal diagonal and connects the **time block** with **global parameters** such as the (runaway) current, toroidal magnetic field strength and q_{95} . Let us focus on the current measurements first. The mode lives inside the CQ as shown in section 4.2. For longer current quench and mode duration, lower subsequent currents are held by runaway electrons (I_{RE} [kA]) and a higher change in current (dI [kA]) will be achieved. This results in high correlation values – positive for the change in current, negative for the runaway current. Another observation of this block is the anti-correlation between the amount of gas injected to trigger the disruption (NZ [bar]) and the start ($t_{\text{IP}} - t_{\text{trigger}}$ [ms]) and end ($t_{\text{end CQ}} - t_{\text{trigger}}$ [ms]) times of the current quench, respectively. The values for the safety factor q_{95} are typically adjusted by varying the plasma current and toroidal magnetic field. As the pre-disruption plasma current is determined by the timing of the MGI, the trigger time shows correlations with B_{tor} and q_{95} . Thereby, earlier injections lead to lower plasma currents, hence higher safety factors.

In **region 3** the correlation between the change in current (dI [kA]) and respective runaway current (I_{RE} [kA]), pre-disruption current (I_{P0} [MA]) and

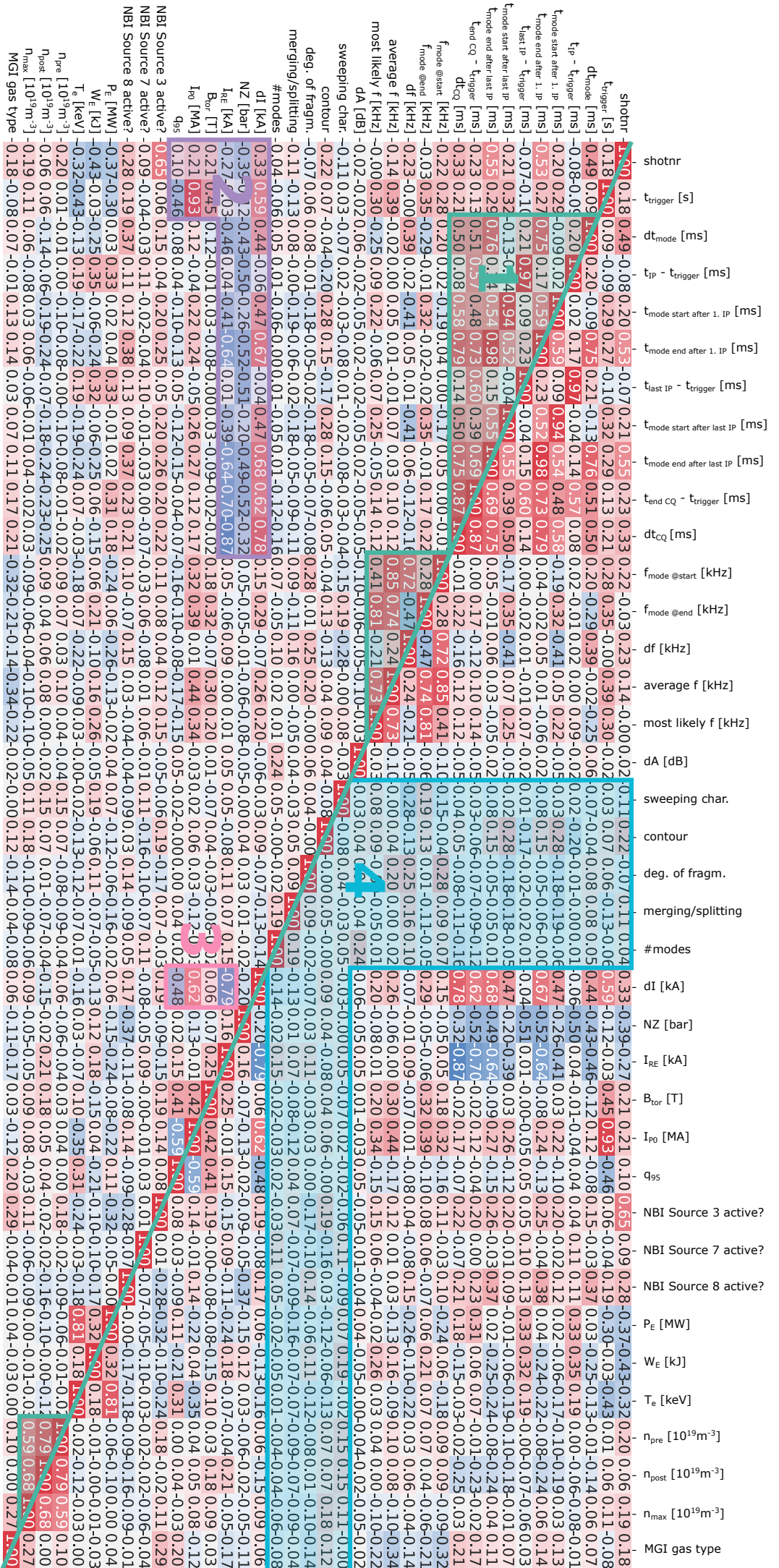


FIGURE 5.3: The correlation matrix with Pearson correlation coefficients.

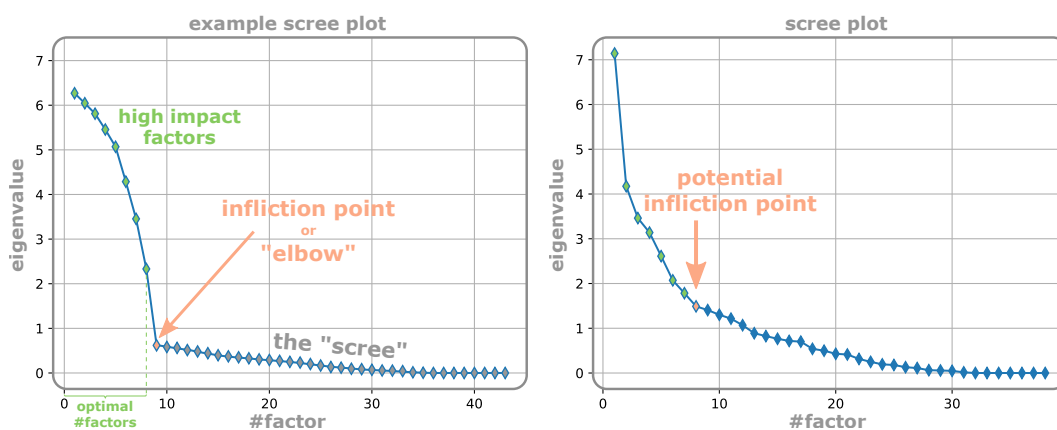
Four regions of interest are highlighted, which are analysed in detail in the text.

q_{95} , are shown. It is expected for dI and I_{RE} to anti-correlate, as well as dI and I_{P0} to correlate, as already indicated in the explanations for region 2. The correlation between q_{95} and dI , can be linked to two different factors. First again q_{95} and I_{P0} are connected as the plasma current is one of the factors determining q . Hence, lower plasma currents often result in higher safety factors and at the same time only allow reduced changes in plasma current. Additionally it is observed for ASDEX Upgrade, that if $q_{95} < 3$ no RE-plateau is forming [64]. This is currently under investigation, but this also contributes to this anti-correlation. As no RE-plateau is present for safety factors below three, the potential change in current is higher.

Region 4 shows the correlation values of the mode characteristics introduced in section 4.1. This region is of special interest, as high correlation results would point towards a connection between the mode behaviour and global parameters. However, we do **not** observe any significant correlations in this region! The higher values within this region, e.g. for the correlation of the change in frequency (df [kHz]) with the sweeping characteristic, can be explained due to the rating system. For this example the sweeping characteristic is granted a number between 1 (*typical*) to 5 (*sinusoidal*) (and 0 for *no mode*). Number 3 is assigned to the behaviour *not chirping*. The anti-correlation is caused by the *typical* sweeping behaviour having a larger change in frequency compared to the *not chirping* one. So by increasing the rating-number from 1 to 3 the change in frequency decreases. Similar effects of the rating system are observed for other characteristics.

5.3.2 Factor analysis

The next step to gain more insight about the underlying correlations inside the database is using the **factor analysis** (FA) method. In this concept multiple observables of the system are reduced to a few underlying factors [65]. These factors are also often referred to as hidden variables as they are not directly measured, but their effect can be visible throughout the observables. This technique is often used e.g. in psychology to describe the connection between different symptoms and their causation. For example "anxiety" could be a factor affecting several symptoms/observables like heartbeat or perspiration [65]. The scree plot is used to determine how many factors are necessary to describe the underlying connections of the system. It received its name as it is supposed to visualize the separation of high impact factors for the system, from the "scree". It typically shows a so-called elbow or inflection point depicted in figure 5.4(a), which acts as the desired separation between factors.



(a) Example scree plot showing an "elbow"

(b) Scree plot of the FA for the database.

FIGURE 5.4: In (a) an example for a typical scree plot is given. The inflection point or "elbow" separates the high impact factors from the "scree". In (b) the scree plot of the FA for our database is depicted. It does not show a clear inflection point, thus the usual, strong separation between the factors. Factor 8 is highlighted as a potential inflection point.

In our case I used factor analysis to find factors, which describe the possible interaction between global parameters and mode characteristics. The results presented in figure 5.4(b) and 5.5 were created with the `FactorAnalyzer` method [66]. The scree plot in figure 5.4(b) does not show a distinct inflection point. This indicates, that the results could not be reduced to a few underlying factors. This could be due to the system being highly complex or the observables not being suited to describe the system well enough with a few observables only. The first 9 factors and their loadings are shown in figure 5.5. Hereby, the factors are sorted by eigenvalues, thus their impact on the system. In the following, I want to present my interpretation for the loadings of each

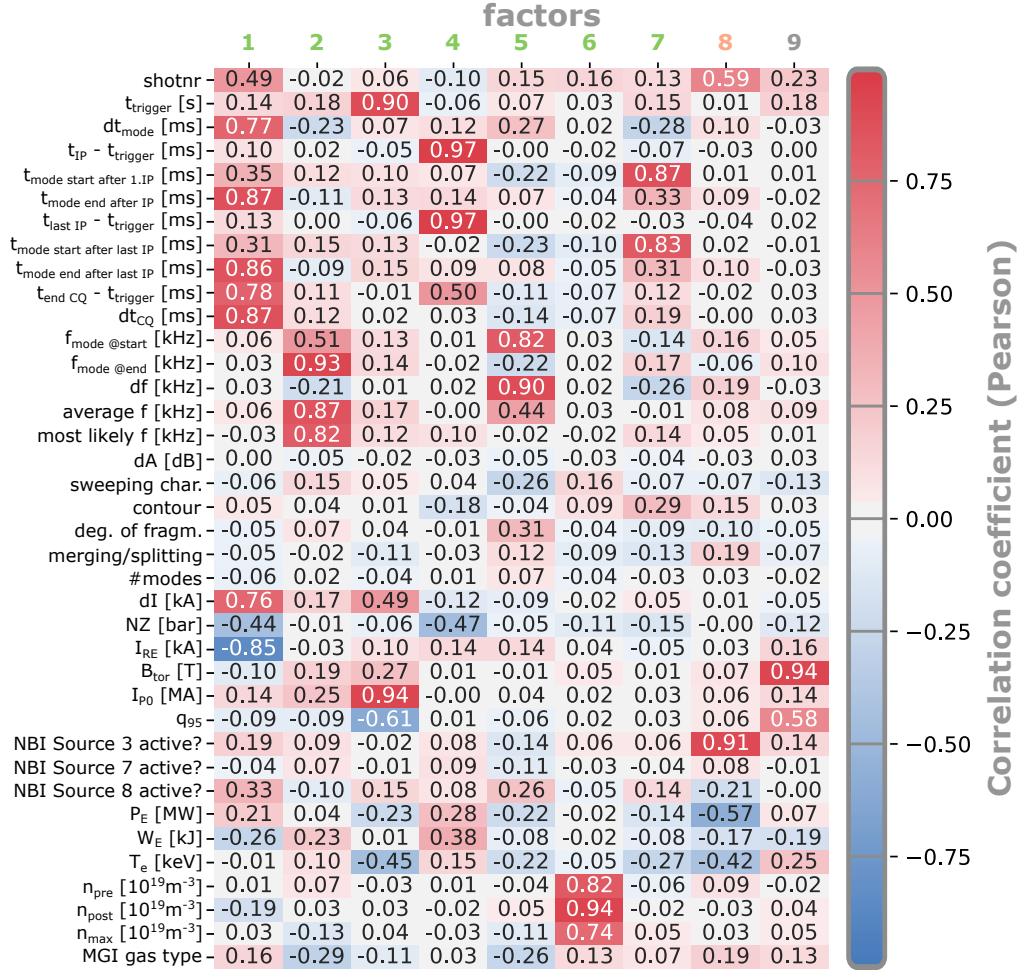


FIGURE 5.5: The loadings for the first 9 factors resulting from the factor analysis.

factor given in figure 5.5. The FA-code does not provide a description or name for each factor – like ”anxiety” from the previous example [65]. Consequently, I will refer to each factor by it’s number. However, I will interpret the internal connection between the observables based on the loadings of each individual factor. Some of these connections might be expected due to prior knowledge or physical dependencies already.

1. The first underlying factor 1 groups mainly the end times of the modes with the current evolution, which was discussed for region 2 in section 5.3.1 already.
2. Here, the frequency properties of the modes are addressed. In section 5.2 a comparison between the average and most likely frequency is provided. Hereby, the end frequency of the mode has the most influence on the average and most likely frequency, respectively. Therefore, the loading for the start frequency is lower compared to the other loadings.

3. This factor illustrates the current ramp-up phase. When the MGI valve is triggered at later times, higher pre-disruption plasma currents and lower safety factors are present. This also affects the possible change in current dI .
4. Higher amounts of gas injected into the chamber will lead to earlier IP-spike times and ultimately also the end time of the current quench reduces.
5. The frequency properties of the mode are again addressed. This time, the start frequency and change in frequency show the highest loadings. Of course the change in frequency is calculated via both – start and end frequency – however, the variation of the start frequency is typically larger compared to the range of end frequencies. Also smaller loadings for the sweeping behaviour and degree of fragmentation and are visible. A possible explanation for this is presented in the following, with discharge #35626 in figure 5.6(a) as an example. This mode was rated as "fragmented" as a small gap exists, between the faint start at 680 kHz and the other part of the mode between 530 – 300 kHz. If this initial fragment of the mode would not be visible – due to a bad SNR or any physical reason – the mode would start at a lower frequency and the start time would be increased. This would also lead to a decreased change in frequency and mode duration, respectively. In addition, without the first fragment of the mode being visible, this mode would not be considered as "fragmented" anymore and the degree of fragmentation would decrease, which could explain the loadings. In addition, the MLF of the discharge #35626 would not be affected by in-/excluding the first part of the mode as it is mainly determined by the end frequency of the mode. This matches the observation of the MLFs-loading close to zero.
6. The plasma density measurements at different times are connected via factor 6. For higher pre-disruption densities also a higher post-disruption and maximum density is expected.
7. Here, mainly the start times of the modes after the first and last IP-spike are connected. As only five discharges within the database contain multiple IP-spikes during incomplete disruptions (see section 4.3), mostly the first IP-spike is also the last IP-spike at the same time. Therefore, the values match most of the time. In addition one can also see smaller loadings for the change in frequency and mode contour characteristic. I want to provide two possible explanations for these loadings. The first covers the ability to determine the correct start time of the mode. For larger mode contour rating numbers – especially the "cloud like" modes, it is increasingly difficult to pin down an exact start and end time of the mode. Therefore, the actual start of the mode might be sometimes earlier than determined by hand. This is illustrated in figure 5.6(b). Here, a

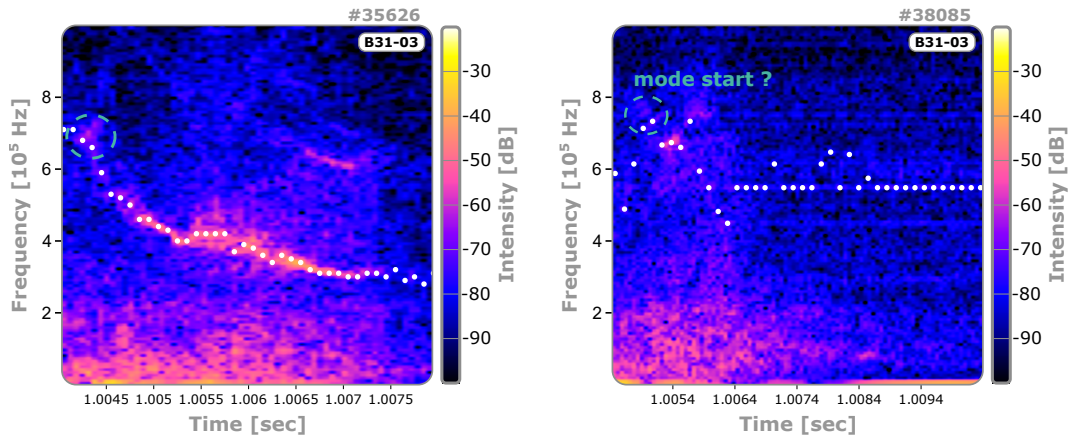
mode labeled as "very cloud like" is shown. Its start time is hard to pin down due to its faint appearance. As the modes often chirp strongest at their start, the change in frequency is affected by this as well. (Very) cloud like modes chirping less than modes with a smaller spectral width, might be another possible explanation.

8. Illustration of changes in the heating schemes over the course of the experimental campaign. Later discharges mostly used the NBI source 3 with different heating schemes compared to the older discharges.
9. The safety factor is directly proportional to the strength of the toroidal magnetic field component, which is illustrated by the loadings for factor 9.

TABLE 5.2: Potential "name" and description of the factors based on their loading.

	Custom "name"	Description of the factor
1	"CQ-extend"	determines the subsequent RE-current
2	"f-plateau"	flattening of the mode frequency chirp towards the end of the mode
3	"MGI trigger timing"	sets post-disruption plasma parameters, such as plasma current
4	"gas penetration"	amount of MGI gas injected directly affects the disruption times
5	"steep mode chirp"	mode sweeping behaviour at the start affects the change in frequency and average frequency
6	"density measurements"	plasma density measurements
7	"mode delay"	timing of the mode start with respect to the (last) IP-spike
8	"experimental setup"	routine of the discharges varied over time
9	"magnetic setup"	connection between B_t and q_{95}

Based on the previous interpretation of the factor loadings, potential "names" and descriptions for each factor are given in table 5.2. However, also for the FA the **mode characteristics** as defined in section 4.1 do **not** show strong loadings within one of those groupings!



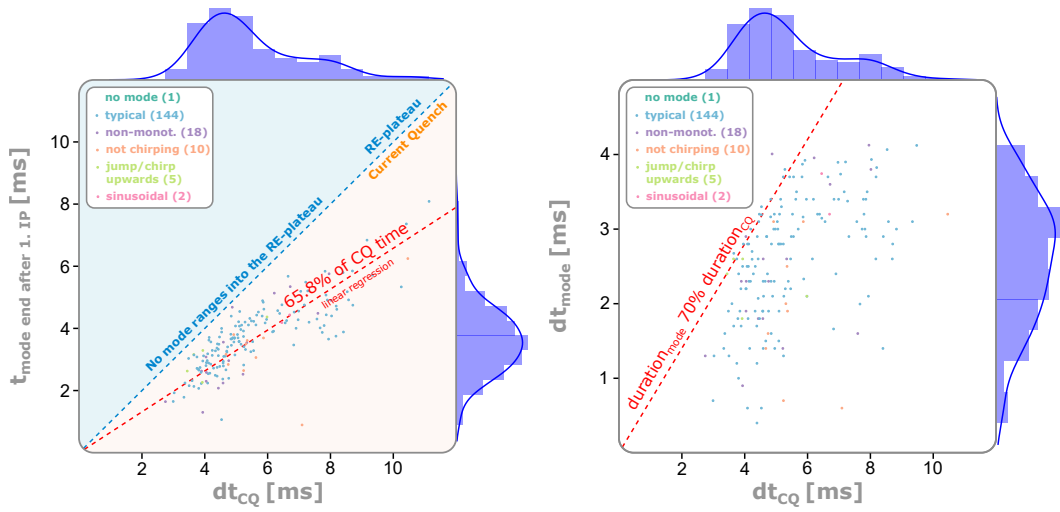
(a) Example mode to illustrate a possible connection between degree of fragmentation and mode start frequency (factor 5).

(b) Unclear start time of the mode for a "very cloud like" mode type (factor 7).

FIGURE 5.6: Example modes illustrating underlying properties affecting the FA.

5.3.3 Regression analysis

While results from the correlation matrix yield the likelihood of a connection between two factors, the regression analysis is used to examine and quantify this relation. For this technique, the factors are plotted against each other and the data is fitted. Most commonly a linear regression is chosen, which uses a linear fit. An example is given in figure 5.7(a) which depicts the **end times** of the mode and the current quench plotted against each other. The linear regression yields that the modes typically last until $\sim 66\%$ of the current quench. The **absolute duration** of the mode and current quench is compared in figure 5.7(b) instead. This plot illustrates, that most modes last for less than 70% of the current quench time. Without using a linear regression of the data, it visualizes similar results compared to the plot in figure 5.7(a). As illustrated by this example, there are multiple options available to gather information from simple scatter-plots. While in some cases a quantitative statement is desirable, in other cases a more qualitative description of the behaviour is more intuitive. This technique is especially useful for hypothesis testing. As shown in section 1.2.2 scientists from DIII-D provide a theoretical connection between the duration of MHD activity and the loss of the initial seed-RE, thus the consequent runaway current I_{RE} . I tested this hypothesis with our database by plotting the RE-current against the duration of the current quench modes, displayed in figure 5.8(a). The trend shows a decreasing runaway current with increasing mode activity time, which would support this thesis. On the other hand one has to keep in mind, that this is just a correlation not necessarily a causation! In figure 5.8(b) the runaway current is plotted against the duration of the current quench, which shows an even more significant trend. However, this correlation can be also explained by the following causal link. The longer the duration of the current quench the larger the time window of potential



(a) Example for a linear regression. Mode end time against current quench duration. (b) Mode duration against duration of the current quench.

FIGURE 5.7: Examples for different investigation methods using scatter-plots. In (a) a linear regression is generated to make quantitative statements, while in (b) the 70 %-line is used just as an indicator for trends within the data. The duration of the current quench is defined with respect to the first IP-spike, thus the bisecting line in (a) represents the transition between the CQ and RE-plateau.

mode activity and also more time for the plasma current to drop to lower values during the current quench. However, we do not observe modes, which last longer than ~ 4 ms, even though the current quench last up to about 10 ms as shown in figure 5.8. The minimum current required on AUG for runaway beams to maintain vertical position control is in the range of 25 – 50 kA, which might explain the discontinuity around 65 kA.

In addition we do **not** observe a decreased runaway current for increased mode amplitudes as shown in figure 5.9. Following the theory on the effect of MHD activity on seed-RE and ultimately the subsequent RE-current, one would expect also a decreasing trend for RE-current with increasing mode amplitude. The regression analysis was also used to investigate the frequency and amplitude evolution within discharges and to compare them to the evolution of other plasma parameters such as density or current. However, up to this point I could **not** find a parameter, which directly correlates with the frequency or amplitude evolution! With our present understanding of the mode's potential origin – which will be presented in chapter 6 – we do not expect a single plasma parameter to determine the modes' time evolution.

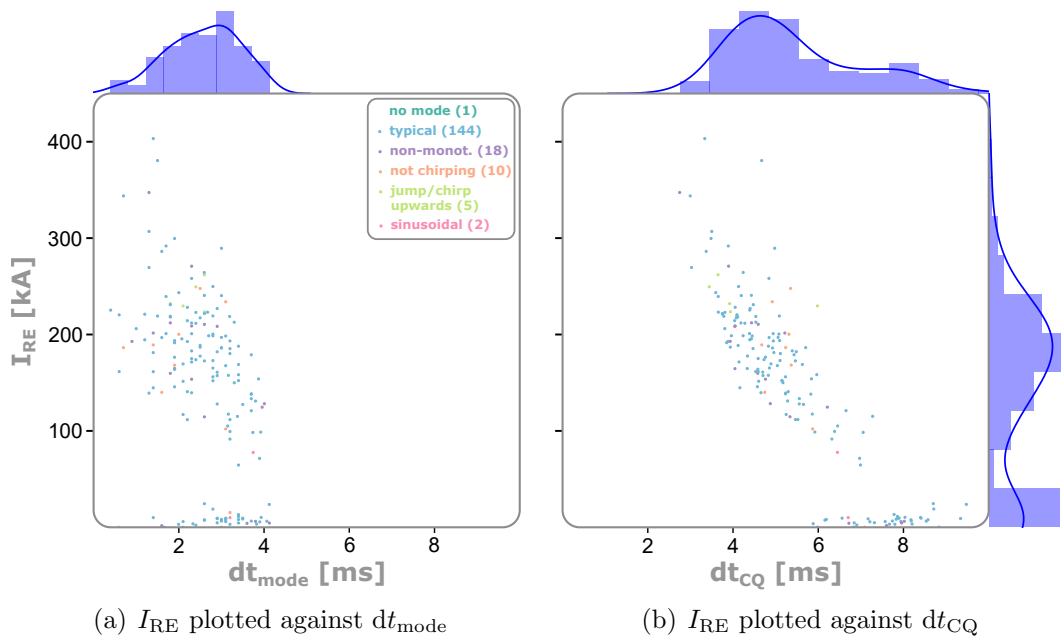


FIGURE 5.8: The runaway current I_{RE} is plotted against the mode duration in (a) and current quench duration in (b), respectively. For (b) this trend seems to be more significant in comparison to (a).

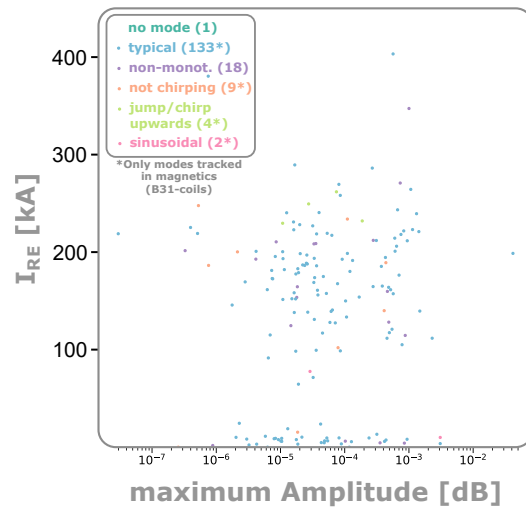


FIGURE 5.9: The runaway current after the current quench phase plotted against the maximum value of the mode amplitude. Only discharges with modes tracked in the magnetics are displayed in this plot. The data does **not** show any trend. Following the contribution from Lvovskiy *et al.* [7], one might expect a decreasing trend of runaway current with increasing maximum mode amplitude, as a decreased seed-RE population is proposed for higher MHD activity.

5.4 Summary of mode characteristics for AUG

Before introducing the present theories behind the CQ-modes, I want to provide a summary of the main take-away points from chapter 4 and 5.

Mode appearance

- The CQ-modes are visible for 179 out of 180 examined discharges, but also appear in natural disruptions.
- For incomplete disruptions, they appear always after the **last** IP-spike.
- They are located **exclusively** inside the CQ as defined in section 1.2.1.

Mode characteristics

- The modes show a monotonic frequency sweeping from higher towards lower frequencies in most cases.
- They possess an increased sweeping rate at the beginning, which flattens over time and the MLF is located around 340 to 370 kHz.
- The typical frequency range for these modes is between 300–800 kHz.
- The different mode characteristics do **not** show significant correlations with the examined global parameters.
- They are visible in the magnetics as well as in the SXR-measurements and are globally coherent.
- For mode numbers the most prominent are $n = 0$ and $n = -4$. In the $n = -4$ case, the mode propagation is in the ion diamagnetic direction.
- Sometimes two mode branches in the same frequency range are visible, which mostly merge at a certain point in time.

Effect on the RE-plateau

For ASDEX Upgrade we observed a trend between the duration of mode activity and subsequent RE-current. On the other hand this relation might be also explained with the duration of the CQ instead. The mode amplitudes measured in the magnetics do not show an effect on the RE-currents.

Comparison with the DIII-D post-disruption modes [7]

For this work, the frequency range up to 1 MHz was analyzed. Therefore, the CQ-modes in AUG might depict only the lowest harmonic visible in figure 1.5, which I would classify as a **typical** sweeping behaviour. Also the highest mode duration in AUG is around 4 ms compared to ~ 8 ms for #177028 in DIII-D.

Chapter 6

Present theories behind the current quench modes

6.1 Compressional Alfvén eigenmodes (CAEs)

In this section, I briefly summarize the paper by Chang Liu *et al.* [9], which proposes the post-disruption modes for DIII-D being CAEs excited by runaway electrons. In theory three characteristic frequencies for REs are prominent, namely the gyrofrequency ω_{ce} , transit and bounce frequency. Given by the condition, that the Alfvén frequency $\omega_A \ll \omega_{ce}$, this interaction is not possible. Also for strongly passing REs, characterized by a small pitch angle, the transit frequency is in the order of 30 MHz, thus does not match the resonance condition. Consequently, the only potential driving source are barely passing or trapped REs, which possess a precession frequency in the CAE frequency range. The necessary amount of trapped runaway electrons could be generated via strong pitch angle scattering with weakly ionized high-Z impurities [28, 67]. Trapped electrons generated by the avalanche mechanism are not expected to contribute, as their energy is not sufficient to resonate with CAEs. The frequency evolution of the modes might be linked to a decreasing ion charge state of argon from $\text{Ar}^{+2} \rightarrow \text{Ar}^{+1}$. Assuming unchanged electron densities, the CAE dispersion relation would yield a decrease in mode frequency by a factor of $\sqrt{2}$. As a constant gas puff during the disruption would provide the constant density levels, the argon charge state would be reduced due to decreasing plasma temperatures. Further simulations for growth rates indicate, that low frequency modes are expected to become unstable first, followed by higher frequent ones. Hereby, the growth rate is a function of I_{RE} , n_e and T_e . This theory shows good agreement with the data from the DIII-D experiments. In the following section, another potential driving mechanism is presented, which is based on the investigations done for the tokamak ASDEX Upgrade.

6.2 Global Alfvén eigenmodes (GAEs)

While compressional Alfvén eigenmodes (CAEs) are hypothesised as a possible explanation for the observations at DIII-D, we focus in the present contribution on another potential driving mechanism for the post-disruption modes – **global Alfvén eigenmodes (GAEs)**.

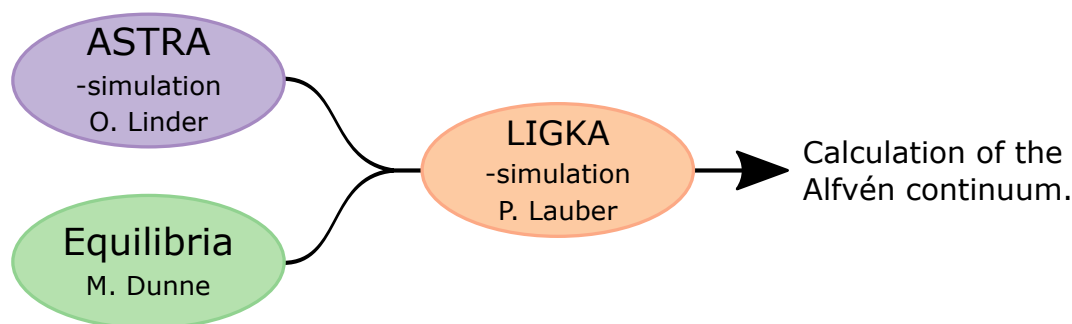


FIGURE 6.1: Profiles from ASTRA simulations and equilibria were fed into LIGKA to calculate the Alfvén continuum.

Oliver Linder created an ASTRA [56] simulation for our favourite discharge #35618. It grants access to the plasma parameters such as the q - or temperature profile. Together with the equilibrium reconstructed by Mike Dunne [68, 69], Philipp Lauber was able to feed that data into LIGKA [39, 40] simulations. With this, he calculated the post-disruption Alfvén continuum which is shown in figure 6.2. In figure 6.2(a)–(e) the results from LIGKA for $n = 0$ are presented for different time points. The plots show the coupled Alfvén continuum (compare figure 1.8(b)) as solid lines. The shaded areas around the central lines show the results for a 20% in-/decrease in ion density. In addition, the first four poloidal mode numbers are highlighted. The ASTRA simulations yield, that the temperature and q profiles are highly peaked, consequently extrema are visible in the Alfvén continuum. As discussed in section 1.3.2, the continuum profiles show maxima instead of the typical minima. As one might expect Alfvénic activity slightly above those maxima, Philipp Lauber did plasma response scans in the LIGKA simulations at these positions, shown in figure 6.2(a). Hereby, excitations by an artificial test-antenna are mimicked and the plasma response to these waves is monitored. Strong reactions of the plasma to these waves hint towards potential modes excited by these waves. The results of the scans above the $m = 2$ or $m = 3$ maximum, are given in figure 6.3. Hereby, the value of the eigenfunctions are plotted against the radial position and the lines represent the different mode numbers of the plasma response. As one might expect, the response is strongest, for the mode number affiliated with the maxima of the Alfvén continuum scanned. Therefore, the strongest response is measured for $m = 2$ and $m = 3$ above the $m = 2$ and $m = 3$ maximum, respectively.

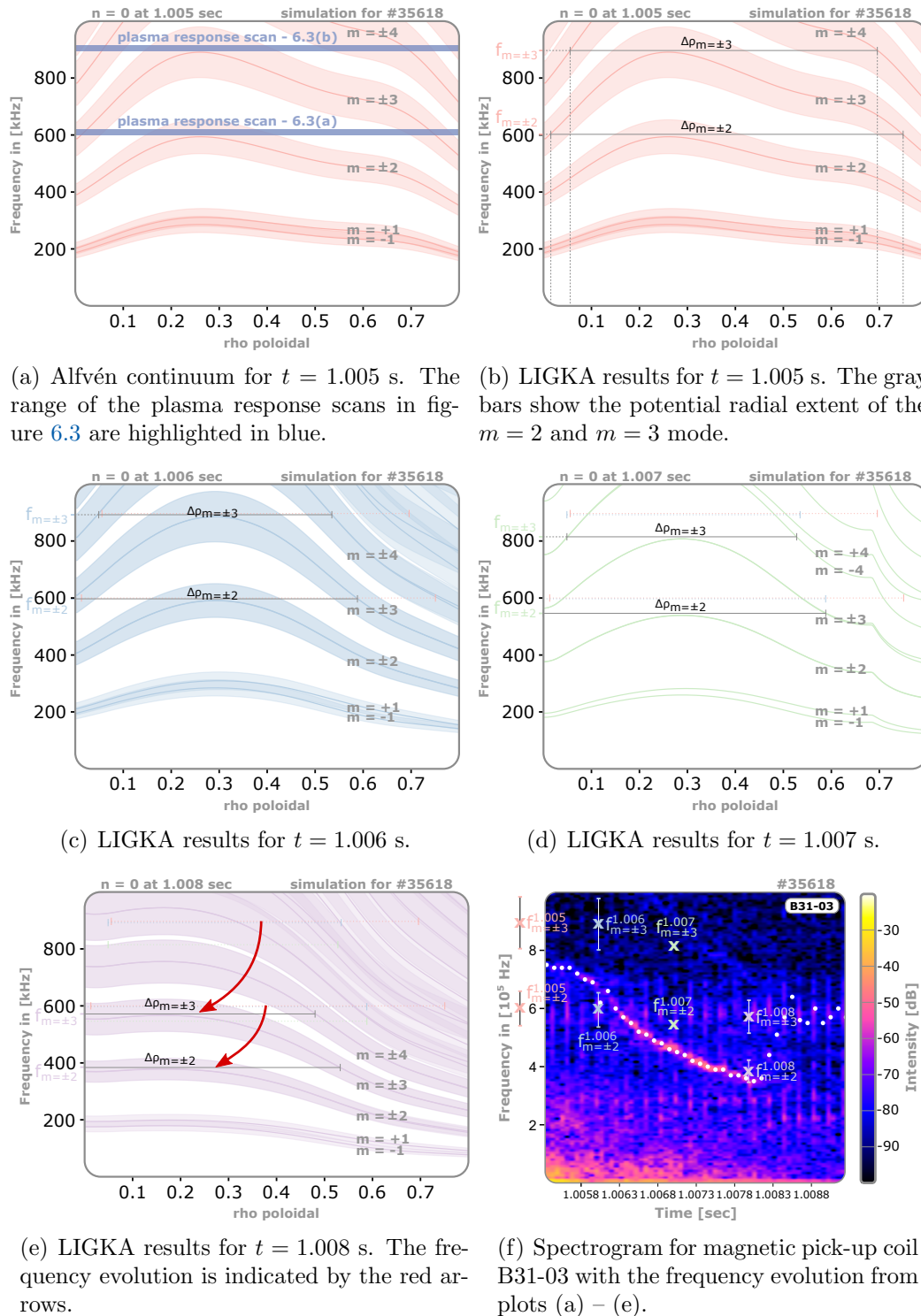
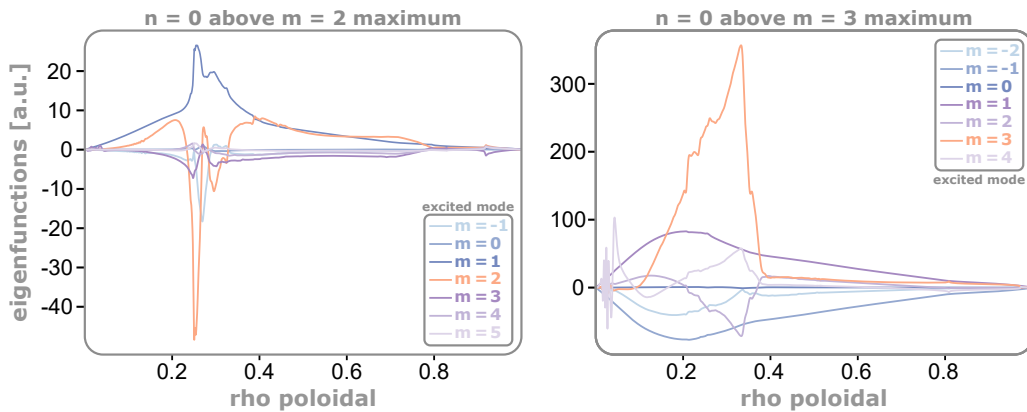


FIGURE 6.2: Results from the LIGKA simulations for discharge #35618. The plots in (a) – (e) show the Alfvén continuum. GAEs can be excited above the maxima, thus their frequency and potential radial extent can be estimated with the help of the plots. The expected frequency evolutions are compared to the experimental result in (f).

As these plots show, we are likely to excite modes (namely GAEs) above these maxima. We can now use this information and track the mode behaviour for different time points shown in figure 6.2. For $t = 1.005$ sec (figure 6.2(b)), I highlighted the modes with $m = 2$ and $m = 3$, which are in a similar frequency range as the mode observed for this discharge. The gray horizontal lines show the potential radial extent of excited modes. At the intersection with the continuum lines, continuum damping will occur, thus is very likely to set a limit to the radial extent. As the mode's frequency will be close to the maxima of the peaked profiles, it is also possible to extract the frequency evolution from the plot. The frequencies, including the error bars, are plotted on top of the spectrogram for the magnetic pick-up coil B31-03 in figure 6.2(f). With time, the profiles evolve and frequencies of the excited waves change, as indicated in the plots (c)–(e). Following the maxima of the profiles, the mode frequency decreases as observed also in the experiment. At $t = 1.008$ sec (figure 6.2(e)) the peaked profiles flatten and the maxima vanish. With this, we also expect the mode to cease, which is in perfect agreement with the experimental results shown in 6.2(f). However, as one can see, the frequency evolutions predicted by the simulation results do not quite match the experimental results. While the $m = 2$ mode would match the observations well for later times, the starting frequency is slightly underestimated. However, the ASTRA simulation for discharge #35618 had been challenging, thus future simulations might increase the precision of the frequency predictions. This first analysis of the CQ-modes does not include investigations for possible mode driving mechanisms. The mode rotates in the ion diamagnetic direction with a mode frequency below the ion cyclotron resonances. Therefore, the modes are likely to be driven by drift reversed trapped electrons or by non-linear excitation mechanisms, such as wave-wave coupling processes. More detailed investigations are performed currently and planned for the future.



(a) LIGKA scans above $m = 2$ maximum. (b) LIGKA scans above $m = 3$ maximum.

FIGURE 6.3: Plasma response scans in the LIGKA simulations. An artificial test-antenna is mimicked, launching waves into the plasma and monitoring the plasma response.

Chapter 7

Summary & Outlook

Disruption avoidance and mitigation of runaway electron formation are necessary steps to reach nuclear fusion power plants based on the tokamak concept. Already for ITER, disruptions depict a significant thread. Therefore, a lot of effort has been put into developing disruption avoidance and mitigation techniques. But besides ever improving technical advances, also investigating the physical properties of disrupting plasmas is key in tackling this issue. As indicated by recent studies from scientists at DIII-D, post-disruption Alfvénic instabilities could be exploited as mitigation tools. The goal of this master’s thesis is to provide further insights on these modes. Therefore, a large database was created by exploring the mode activity in experiments executed over the course of six years.

With my new tools, I was able to trace the mode’s frequency and amplitude evolution, which opened up new possibilities to observe the underlying physics. I introduced my personal characterization system, which covers the sweeping behaviour of the mode, its spectral width and degree of fragmentation. Whether the mode splits into separate branches or emerges from them, was also investigated as well as the number of modes counted. The overwhelming fraction of modes start at higher frequencies and chirp continuously towards lower ones. They depict a stronger frequency chirp at the beginning of the mode, which flattens over time. The modes appear exclusively during the current quench and end before the subsequent RE-plateau arises. However, no mode had been observed in between separate IP-spikes during incomplete disruptions, but rather start after the **last** IP-spiked had occurred. The analysis of the SXR measurements yielded – in contrast to previous expectations – strong amplitudes in the plasma edge region. Further, the modes themselves are globally coherent, as they are visible in almost every magnetic coil within the chamber as well as LOSs of the SXR measurements. However, determining the mode number turned out to be very challenging, as mode numbers seem to be more like a zoo of many different ones. The most prominent toroidal mode numbers seem to be $n = 0$ and $n = -4$.

If the modes truly affect the formation of the subsequent runaway electron beam, exploiting this effect by externally driving these modes unstable might

be desirable. For this to work, the frequency range for excitations of these modes, has to be known. The "most likely frequency" of the modes represents the frequency range the mode is observed at for the longest duration. Considering 179 discharges, the most prominent frequencies had been found to be 340 and 370 kHz, respectively.

On the present database, three statistical analysis methods were applied. With the help of a large correlation matrix, four regions of interest were highlighted and the correlation results within analyzed in detail. Factor analysis was used to sort the observables and create subsets of measurement outcomes. With this, a few underlying mechanisms were pointed at, such as the connection between start and end times of the current quench and global parameters, like the amount of gas injected into the chamber during MGI. It also indicated potential problems, which arise due to the mode characterization system. However, despite a large data set, **no significant correlations** between mode characteristics and global parameters had been found during the statistical analysis process. Most correlations within the database can be explained by prior knowledge of the underlying physics or experimental setup.

A brief hypothesis testing on the mechanism proposed by Lvovskiy *et al.* [7] was performed. It was claimed, that increasing mode activity during the disruption phase will lead to reduced strength of the subsequent RE-plateau. While a decreasing trend of the RE-current with increase in mode duration is also observed in AUG, the mode amplitude does **not** show any effect. Following this, the trend might be explained by an extended **current quench** duration instead.

In the last chapter, the current theories behind the modes are presented. As the modes show an Alfvénic behaviour, we propose global Alfvén eigenmodes as the underlying drive. The evolution of the Alfvén continuum – caused by changes of plasma properties during the disruption – can be used to explain the observations. Not only the frequency sweep directly follows this implication, but also the duration of the modes is in perfect agreement with the expectations from the simulation performed. Therefore, this theory is a reasonable alternative compared to the drive by compressional Alfvén eigenmodes proposed by Chang Liu *et al.* [9]. However, it is important to emphasize, that the modes observed in AUG and DIII-D could also be caused by different underlying mechanisms.

While exploiting the underlying physics behind these modes might enable advanced disruption mitigation techniques for future fusion devices, we are far from understanding them. Consequently, it is important to continue studying the current quench modes. Experiments on external mode drive are planned for AUG in the upcoming campaigns, which might grant new and important insights on this subject.

Bibliography

- [1] F. F. Chen, An indispensable truth: how fusion power can save the planet (Springer Science & Business Media, New York, 2011).
- [2] F. Flakus, J. Cleveland and T. Dolan, IAEA Bulletin **37**, 22 (1995).
- [3] B. Sieglin *et al.*, Plasma Physics and Controlled Fusion **55**, 124039 (2013).
- [4] T. Hender *et al.*, Nuclear Fusion **47**, S128 (2007).
- [5] E. M. Hollmann *et al.*, Physics of Plasmas **22**, 021802 (2015).
- [6] M. Lehnen *et al.*, Journal of Nuclear Materials **463**, 39 (2015).
- [7] A. Lvovskiy *et al.*, Plasma Physics and Controlled Fusion **60**, 124003 (2018).
- [8] C. Paz-Soldan, The Measurement and Control of Relativistic Electrons in Tokamaks (Journal of Plasma Physics Colloquium, online seminar, 2020).
- [9] C. Liu *et al.*, Nuclear Fusion **61**, 036011 (2021).
- [10] Lexikon der Physik - Tokamak, <https://www.spektrum.de/lexikon/physik/tokamak/14587>, accessed: 2021-02-15.
- [11] W. Stieler, Startschuss für Fusionsreaktor, <https://www.heise.de/newsticker/meldung/Startschuss-fuer-Fusionsreaktor-120106.html>, upload: 2006-11-22, accessed: 2021-02-15.
- [12] I. Milch, Kultur und Technik – das Magazin aus dem Deutschen Museum **31**, 46 (2007).
- [13] D. Clery, After ITER, Many Other Obstacles for Fusion Power, <https://www.sciencemag.org/news/2013/01/after-iter-many-other-obstacles-fusion-power>, upload: 2013-01-17, accessed: 2021-02-15.
- [14] C. Jeffrey, Wendelstein 7-x stellarator puts new twist on nuclear fusion power, <https://newatlas.com/wendelstein7x-fusion-stellarator-plasma-tests/40014/>, upload: 2015-10-25, accessed: 2021-02-15.

- [15] J. Ongena, R. Koch, R. Wolf and H. Zohm, *Nature Physics* **12**, 398 (2016).
- [16] G. Grieger and I. Milch, *Physikalische Blätter* **49**, 1001 (1993).
- [17] 3D image of a Tokamak, https://acee.princeton.edu/wp-content/uploads/2016/07/Tokamak3D_englisch_08.png, accessed: 2020-12-01.
- [18] U. Stroth, *Plasmaphysik - Phänomene, Grundlagen und Anwendungen*, 2nd ed. (Springer Spektrum, Berlin, 2018).
- [19] S. Günter, *Plasmaphysik und Fusionsforschung* (Max-Planck Institut für Plasmaphysik and TUM, Garching, Germany, 2019).
- [20] A. Bock *et al.*, *Physics of Plasmas* **25**, 056115 (2018).
- [21] J. D. Lawson, *Proceedings of the Physical Society. Section B* **70**, 6 (1957).
- [22] M. Shimada *et al.*, *Nuclear Fusion* **47**, S1 (2007).
- [23] AUG-Intranet: Detailed description of ASDEX Upgrade, <https://www.aug.ipp.mpg.de/wwwaug/documentation/physics/techdata.shtml>, last update: 2020-09-28, accessed: 2021-02-25.
- [24] R. Neu, *Physica Scripta* **T123**, 33 (2006).
- [25] R. Neu *et al.*, *Plasma Physics and Controlled Fusion* **49**, B59 (2007).
- [26] P. de Vries *et al.*, *Nuclear Fusion* **51**, 053018 (2011).
- [27] R. G. Kleva and P. N. Guzdar, *Physics of Plasmas* **8**, 103 (2001).
- [28] B. N. Breizman, P. Aleynikov, E. M. Hollmann and M. Lehnen, *Nuclear Fusion* **59**, 083001 (2019).
- [29] M. Rosenbluth and S. Putvinski, *Nuclear Fusion* **37**, 1355 (1997).
- [30] G. F. Matthews *et al.*, *Physica Scripta* **T167**, 014070 (2016).
- [31] V. Sizyuk and A. Hassanein, *Nuclear Fusion* **49**, 095003 (2009).
- [32] G. Pautasso *et al.*, *Nuclear Fusion* **60**, 086011 (2020).
- [33] E. M. Hollmann *et al.*, *Nuclear Fusion* **53**, 083004 (2013).
- [34] G. Pautasso *et al.*, *Plasma Physics and Controlled Fusion* **59**, 014046 (2016).
- [35] D. Pace *et al.*, *Review of Scientific Instruments* **87**, 043507 (2016).
- [36] H. Alfvén, *Nature* **150**, 405 (1942).
- [37] P. W. Lauber, *Physics Reports* **533**, 33 (2013).

- [38] W. W. Heidbrink, *Physics of Plasmas* **15**, 055501 (2008).
- [39] P. W. Lauber, Dissertation, Technische Universität München, München, 2003.
- [40] P. W. Lauber, S. Günter, A. Könies and S. Pinches, *Journal of Computational Physics* **226**, 447 (2007).
- [41] S. D. Pinches, Ph.D. thesis, University Nottingham, 1998.
- [42] K. Appert, R. Gruber, F. Troyon and J. Vaclavik, *Plasma Physics* **24**, 1147 (1982).
- [43] S. Mahajan and D. W. Ross, *The Physics of fluids* **26**, 2561 (1983).
- [44] N. Gorelenkov and C. Cheng, *Nuclear fusion* **35**, 1743 (1995).
- [45] E. Fredrickson, N. Gorelenkov and J. Menard, *Physics of plasmas* **11**, 3653 (2004).
- [46] J. B. J. baron Fourier, *Théorie analytique de la chaleur* (F. Didot, New York Public Library, New York, 1822).
- [47] M. Stéphane, *A Wavelet Tour of Signal Processing*, 3rd ed. (Academic Press, Boston, 2009).
- [48] D. Gabor, *Journal of the Institution of Electrical Engineers-Part III: Radio and Communication Engineering* **93**, 429 (1946).
- [49] P. Welch, *IEEE Transactions on Audio and Electroacoustics* **15**, 70 (1967).
- [50] V. Igochine, *Active Control of Magneto-hydrodynamic Instabilities in Hot Plasmas* (Springer-Verlag Berlin Heidelberg, London, England, 2015), No. 1.
- [51] I. H. Hutchinson, *Principles of Plasma Diagnostics*, 2 ed. (Cambridge University Press, Cambridge, 2002).
- [52] L. Horváth *et al.*, *Plasma Physics and Controlled Fusion* **57**, 125005 (2015).
- [53] AUG-Intranet: The MIRNOV-diagnostic (MTR), https://www.aug.ipp.mpg.de/aug/local/aug_only/magnetics/, last update: 2017-02-06, accessed: 2020-11-16.
- [54] AUG-Intranet: Soft X-ray diagnostic in ASDEX Upgrade, <https://www.aug.ipp.mpg.de/~vgi/SXR.html>, accessed: 2020-11-16.
- [55] A. Richardson, Naval Research Laboratory Washington, DC (2019).
- [56] O. Linder *et al.*, *Nuclear Fusion* **60**, 096031 (2020).

- [57] E. W. Dijkstra, *Numerische Mathematik* **1**, 269 (1959).
- [58] `scipy.signal.welch` documentation, <https://docs.scipy.org/doc/scipy/reference/generated/scipy.signal.welch.html>, last updated: 2020-11-04, accessed: 2020-12-31.
- [59] pseudorandomcoder, *Serious Deep Coding: Dijkstra's Algorithm in Python and Modeling Software Career Progress*, <https://www.youtube.com/watch?v=f7xEG18FlgA>, upload: 2018-07-09, accessed: 2020-11-16.
- [60] A. Magyarkuti, Az ASDEX Upgrade tokamakon detektált plazmaközepi MHD módusok frekvenciamodulációjának kinyerése lágy röntgen jelekből. (Scientific Student Conference (TDK), Budapest University of Technology and Economics, Budapest, Hungary, 2009).
- [61] `matplotlib.axes.Axes.specgram` documentation, https://matplotlib.org/3.3.3/api/_as_gen/matplotlib.axes.Axes.specgram.html, last update: 2020-11-12, accessed: 2021-01-21.
- [62] `pandas.DataFrame.corr` documentation, <https://pandas.pydata.org/pandas-docs/stable/reference/api/pandas.DataFrame.corr.html>, accessed: 2020-12-22.
- [63] SPSS tutorials: Pearson Correlation, <https://libguides.library.kent.edu/SPSS/PearsonCorr>, accessed: 2020-12-14.
- [64] G. Papp *et al.*, The effect of high-Z material injection on runaway electron dynamics. (46th EPS Conference on Plasma Physics, Milan, Italy, 2019).
- [65] A. G. Yong and S. Pearce, *Tutorials in quantitative methods for psychology* **9**, 79 (2013).
- [66] `FactorAnalyzer` documentation, <https://factor-analyzer.readthedocs.io/en/latest/index.html>, accessed: 2020-12-15.
- [67] L. Hesslow *et al.*, *Phys. Rev. Lett.* **118**, 255001 (2017).
- [68] P. J. Mc Carthy, *Physics of Plasmas* **6**, 3554 (1999).
- [69] M. Dunne *et al.*, *Nuclear Fusion* **52**, 123014 (2012).